ApJ. accepted
Preprint typeset using LaTeX style emulateapj v. 12/16/11

arXiv:2105.01681v3 [astro-ph.GA] 22 Jul 2021

HI-TO-H_2 TRANSITIONS IN DUST-FREE INTERSTELLAR GAS

Amiel Sternberg[1, 2, 3⋆], Alon Gurman[1], & Shmuel Bialy[4]

ApJ. accepted

ABSTRACT

We present numerical computations and analysis of atomic to molecular (HI-to-H_2) transitions in cool ($\sim$100 K) low-metallicity dust-free (primordial) gas, in which molecule formation occurs via cosmic-ray driven negative ion chemistry, and removal is by a combination of far-UV photodissociation and cosmic-ray ionization and dissociation. For any gas temperature, the behavior depends on the ratio of the Lyman-Werner (LW) band FUV intensity to gas density, $I_{\rm LW}/n$, and the ratio of the cosmic-ray ionization rate to the gas density, ζ/n. We present sets of HI-to-H_2 abundance profiles for a wide range of ζ/n and $I_{\rm LW}/n$, for dust-free gas. We determine the conditions for which H_2 absorption line self-shielding in optically thick clouds enables a transition from atomic to molecular form for ionization driven chemistry. We also examine the effects of cosmic-ray energy losses on the atomic and molecular density profiles and transition points. For a unit Galactic interstellar FUV field intensity ($I_{\rm LW}=1$) with LW flux 2.07×10^7 photons cm^{-2} s^{-1}, and a uniform cosmic-ray ionization rate $\zeta=10^{-16}$ s^{-1}, an HI-to-H_2 transition occurs at a total hydrogen gas column density of 4×10^{21} cm^{-2}, within 3×10^7 yr, for a gas volume density of $n=10^6$ cm^{-3} at 100 K. For these parameters, the dust-free limit obtains for a dust-to-gas ratio $Z'_d\lesssim10^{-5}$, which may be reached for overall metallicities $Z'\lesssim0.01$ relative to Galactic solar values.

Subject headings: Interstellar medium (847) – Photodissociation regions (1223) – Cosmic rays (329)

1. INTRODUCTION

Atomic to molecular hydrogen (HI-to-H_2) transitions are of fundamental importance for the structure of the interstellar medium (ISM) in galaxies (Sternberg et al. 2014, hereafter S14). Numerous observational studies show that dense molecular gas is closely correlated with star-formation, from sub-pc to kpc scales, and across cosmic time from low to high redshifts (Tacconi et al. 2020). H_2 formation may promote cooling and cloud fragmentation, and/or it may be accelerated in gravitationally collapsing regions where the gas becomes dense, and optically thick to destructive radiation fields.

In star-forming galaxies, especially Milky Way like systems containing diffuse to dense interstellar gas clouds, it is well established that hydrogen molecules are generally formed on the surfaces of dust grains (Gould & Salpeter 1963; Jura 1974; Le Bourlot et al. 2012; Girichidis et al. 2020). The formation efficiencies (via chemisorption and/or physisorption) depend on the solid-state dust compositions, the gas and grain temperatures, and the overall gas-to-dust mass ratios (Cuppen et al. 2010; Wakelam et al. 2017). For systems in which the heavy element and dust abundances are very low, or if the grain surface temperatures are too high, the grain induced formation rates vanish, and molecules are instead formed by gas phase processes, especially via the H^- negative ion intermediary (McDowell 1961; de Jong 1972; Dalgarno & McCray 1973; Glover 2003; Larsson et al. 2012). For example, gas phase production of H_2 may dominate in protoplanetary disks where high temperatures inhibit gas-grain sticking (Glassgold et al. 2004), or in dust-poor outflow jets from protostars (Tabone et al. 2020). In metal rich disks and jets, gas phase H_2 formation enables synthesis of heavy molecules (CO, OH, etc.) via the usual neutral-neutral and ion-molecule reactions, as occurs in dusty clouds (Herbst & Klemperer 1973; Sternberg & Dalgarno 1995; Tielens 2013; van Dishoeck 2014; Bialy & Sternberg 2015; Öberg & Bergin 2021). Atomic to molecular conversion for dust-free conditions may also be important in low-metallicity damped Lyman-α absorbers (DLAs) (Ranjan et al. 2018) or perhaps in dense condensations within cool filaments in the circumgalactic medium (CGM) of galaxies and/or the cosmic web.

Gas phase H_2 formation was critically important in the dust-free early Universe where even minute amounts of H_2 enabled cooling to low ($\sim$ 100 K) temperatures, reduction of the Jeans masses, and the collapse of the first objects (Peebles & Dicke 1968; Tegmark et al. 1997; Lepp et al. 2002; Haiman 2016). Feedback in the form of photodissociating Lyman-Werner (LW) band radiation from the first stars plausibly regulated the early star-formation rates and the formation of seed black holes (Haiman et al. 1997; Visbal et al. 2014; Latif et al. 2014; Wolcott-Green et al. 2021). HI-to-H_2 conversion for Galactic conditions, and the structures of photodissociation regions (PDRs) in dense Milky Way molecular clouds are well understood (Federman et al. 1979; Tielens & Hollenbach 1985; Black & van Dishoeck 1987; Röllig et al. 2006; McKee & Krumholz 2010; Sternberg et al. 2014). But how do analogous HI-to-H_2 PDR transitions occur for early Universe conditions?

The astrophysics of HI-to-H_2 conversion in the dusty interstellar medium (ISM) was reviewed in S14. That paper also presented numerical computations and ana-

⋆asternberg@flatironinstitute.org
[1] School of Physics and Astronomy, Tel Aviv University, Ramat Aviv 69978, Israel
[2] Center for Computational Astrophysics, 162 5th Ave., New York, NY, 10010
[3] Max-Planck-Institut für extraterrestrische Physik (MPE), Giessenbachstr., 85748 Garching, FRG
[4] Center for Astrophysics | Harvard & Smithsonian, 60 Garden st., Cambridge, MA, 02138

lytic theory for HI-to-H_2 transitions and the build up of photodissociated HI columns in dusty FUV-irradiated molecular cloud surfaces (PDRs). In Bialy & Sternberg (2016, hereafter BS16) we presented an analytic procedure for generating depth-dependent HI/H_2 density profiles, again for dusty clouds, for a wide range of assumed gas-to-dust mass ratios. In all of these computations, dust plays a dual role, (a) in providing the molecular formation sites, and (b) as shielding agents via FUV absorption (and scattering). Both roles, especially shielding, enable the atomic to molecular conversions.

In this paper, we extend the methodology presented in S14 and BS16 for a theoretical study of atomic-to-molecular transitions in dust-free environments. We consider simple idealized steady-state models consisting of FUV irradiated plane parallel isothermal constant density slabs, in which H_2 formation is via ionization driven gas phase processes, and attenuation of the photodissociation rate is by H_2 absorption-line self-shielding only. This as opposed to dusty clouds in which H_2 is formed on dust grains, and shielding includes dust absorption in addition to molecular self-shielding. We assume that the cloud ionization is provided by a flux of (low-energy) penetrating cosmic-ray particles. We do not consider irradiation by X-rays. We assume that the fractional ionizations are not affected by the presence of any heavy elements ("metals"), or by interactions with dust grains or large molecules such as polycyclic aromatic hydrocarbons (PAHs). Ionization drives the molecular hydrogen formation chemistry everywhere in the cloud, including the outer photodissociation regions (PDRs) and the inner optically thick cosmic-ray zones (CRZs). Ionization also serves as an H_2 removal mechanism in the cosmic-ray zones. We present analytic and numerical computations for the HI and H_2 density profiles for the dust-free conditions.

In §2, we present our model ingredients. This includes a review of the metal-free hydrogen-helium chemical network, and a discussion of FUV photodissociation, H_2 self-shielding, and cosmic-ray propagation. In §3 we present an analytic model for the expected atomic to molecular profiles, and dependence on the FUV field strength, gas density, and ionization rate. We also consider the timescales. We develop expressions for the total HI column densities in the PDRs and CRZs, as functions of FUV radiation intensity, cosmic-ray ionization rate, gas density, and temperature. In §4 we present numerical computations for the atomic and molecular density profiles and transition points for dust free conditions. These computations include a fiducial model and a paramter study for a range of FUV intensities, gas densities, and ionization rates. We compare to our analytic description. We summarize in §5.

2. MODEL INGREDIENTS

2.1. *Chemistry*

We consider a steady-state between formation of H_2 via cosmic-ray driven negative ion chemistry, and destruction by FUV photodissociation and cosmic-ray ionization and dissociation, in a dust-free environment.

Our metals-free hydrogen and helium chemical networks are shown in Figure 1. The reactions and rate coefficients are listed in Tables 1, and 2. We solve for

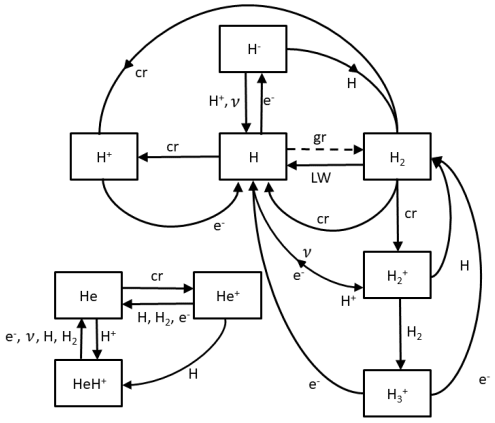


FIG. 1.— Schematic of the metals-free two-body reaction gas-phase hydrogen-helium network. The dashed arrow indicates grain-surface formation of H_2 that we are explicitly excluding.

the steady state abundances of H, H_2, H^-, H^+, H_2^+, H_3^+, He, He^+, HeH^+, and electrons. No heavy elements are included. The species abundances vary with cloud depth as the photodissociating FUV radiation is absorbed by the H_2, and as cosmic-ray energy losses reduce the ionization rates.

2.1.1. *Hydrogen Network*

Molecular hydrogen is formed mainly via the well-known two-step catalytic sequence, starting with (slow) radiative attachment,

$$\mathrm{H} + \mathrm{e} \rightarrow \mathrm{H}^- + \nu \qquad \text{(R1)}$$

followed by (rapid) associative detachment

$$\mathrm{H}^- + \mathrm{H} \rightarrow \mathrm{H}_2 + \mathrm{e} \quad . \qquad \text{(R2)}$$

In regions with large fractional ionizations and/or low gas densities this sequence may be moderated by mutual neutralization

$$\mathrm{H}^- + \mathrm{H}^+ \rightarrow \mathrm{H} + \mathrm{H} \quad , \qquad \text{(R3)}$$

and photodetachment

$$\mathrm{H}^- + \nu \rightarrow \mathrm{H} + \mathrm{e} \quad . \qquad \text{(R4)}$$

Photodetachment is by radiation shortward of the 1.6 μm ($E > 0.75$ eV) infrared threshold. For the high gas density parameter space we consider in this paper, [R3] and [R4] are slow in comparison to [R2], and do not reduce the molecular formation efficiencies. An additional H_2 formation route is radiative association

$$\mathrm{H} + \mathrm{H}^+ \rightarrow \mathrm{H}_2^+ + \nu \qquad \text{(R5)}$$

followed by charge transfer

$$\mathrm{H}_2^+ + \mathrm{H} \rightarrow \mathrm{H}_2 + \mathrm{H}^+ \quad . \qquad \text{(R6)}$$

This channel is generally a minor contributor.

The H_2 formation sequence, [R1] and [R2], requires electrons, and these are produced by an ionization source that we assume are non-thermal cosmic-ray particles,

$$\mathrm{H} + \mathrm{cr} \rightarrow \mathrm{H}^+ + \mathrm{e} \qquad \text{(R7)}$$

TABLE 1
RATE COEFFICIENTS

Reaction	Rate Coefficient (cm^3 s^{-1})	Index	Reference
$H + e \rightarrow H^- + \nu$	$1.67 \times 10^{-16} T_2^{0.64} e^{-0.092/T_2}$	R1	M13, Stancil & Dalgarno (1998)
$H^- + H \rightarrow H_2 + e$	$6.63 \times 10^{-9} T_2^{-0.39} e^{-0.394/T_2}$	R2	M13, Bruhns et al. (2010)
$H^- + H^+ \rightarrow H + H$	$1.30 \times 10^{-7} T_2^{-0.50}$	R3	M13, Harada & Herbst (2008)
$H^+ + H \rightarrow H_2^+ + \nu$	$2.31 \times 10^{-19} T_2^{1.50}$	R5	N20, Ramaker & Peek (1976)
$H + H_2^+ \rightarrow H_2 + H^+$	6.40×10^{-10}	R6	M13, Karpas et al. (1979)
$H^+ + e \rightarrow H + \nu$	$7.98 \times 10^{-12} T_2^{-0.75}$	R9	M13, Prasad & Huntress (1980)
$H_2^+ + H_2 \rightarrow H_3^+ + H$	2.08×10^{-9}	R10	M13, Theard & Huntress (1974)
$H_2^+ + e \rightarrow H + H$	$1.89 \times 10^{-8} T_2^{-0.40}$	R11	N20, Schneider et al. (1994)
$H_3^+ + e \rightarrow H + H + H$	$7.72 \times 10^{-8} T_2^{-0.52}$	R13	M13, McCall et al. (2004)
$H_3^+ + e \rightarrow H_2 + H$	$4.14 \times 10^{-8} T_2^{-0.52}$	R14	M13, McCall et al. (2004)
$H + He^+ \rightarrow He + H^+$	$9.12 \times 10^{-16} T_2^{0.25}$	R21	M13, Stancil et al. (1998)
$H_2 + He^+ \rightarrow He + H_2^+$	7.20×10^{-15}	R22	M13, Barlow (1984)
$H_2 + He^+ \rightarrow He + H + H^+$	$3.70 \times 10^{-14} e^{-0.35/T_2}$	R23	M13, Barlow (1984)
$He^+ + e \rightarrow He + \nu$	$9.28 \times 10^{-12} T_2^{-0.50}$	R24	M13, Ercolano & Storey (2006)
$H + He^+ \rightarrow HeH^+ + \nu$	1.44×10^{-16}	R25	N20, based on Vranckx et al. (2013)
$H^+ + He \rightarrow HeH^+ + \nu$	$1.77 \times 10^{-18} T_2^{-1.25}$	R26	N20, Juřek et al. (1995)
$H + HeH^+ \rightarrow He + H_2^+$	1.70×10^{-9}	R27	N20, Esposito et al. (2015)
$H_2 + HeH^+ \rightarrow He + H_3^+$	1.50×10^{-9}	R28	M13, Bohme et al. (1980), Herbst et al. (1975)
$HeH^+ + e \rightarrow He + H$	$4.31 \times 10^{-9} T_2^{-0.50}$	R29	N20, Novotný et al. (2019)

Rate coefficients for the two-body reactions in our network, operating in the low-temperature ($T \lesssim 10^3$ K) regime. Here, $T_2 = T/(100\ \mathrm{K})$. The rate coefficients are from the UMIST2012 compilation (M13; McElroy et al. 2013), or the more recent (N20; Neufeld et al. 2020) compilation mainly for the helium chemistry. We list the primary references as given by M13 and N20.

TABLE 2
COSMIC RAY RATES

Reaction	Relative Rate	Index
$H + cr \rightarrow H^+ + e$	0.46	R7
$H_2 + cr \rightarrow H_2^+ + e$	0.96	R8
$H_2 + cr \rightarrow H + H$	0.7	R15
$H_2 + cr \rightarrow H + H^+ + e$	0.04	R16
$He + cr \rightarrow He^+ + e$	0.5	R20

Cosmic ray reaction rates relative to the total H_2 cosmic-ray ionization rate ([R8]+[R16]).

and

$$H_2 + cr \rightarrow H_2^+ + e \quad . \tag{R8}$$

Cosmic-ray ionization is also the main source of protons. The protons are removed by slow radiative recombination

$$H^+ + e \rightarrow H + \nu \quad . \tag{R9}$$

The H_2^+ ions undergo rapid abstraction

$$H_2^+ + H_2 \rightarrow H_3^+ + H \quad . \tag{R10}$$

These reactions, together with charge transfer [R6] are the primary removal channels for the H_2^+ ions. Dissociative recombination

$$H_2^+ + e \rightarrow H + H \quad , \tag{R11}$$

is a minor removal process unless the fractional ionizations become large. The H_2^+ may also be removed by far-UV photons

$$H_2^+ + \nu \rightarrow H + H^+ \quad , \tag{R12}$$

but this is a minor removal channel in our parameter space.

The saturated H_3^+ ions produced by [R10] recombine quickly with electrons

$$H_3^+ + e \rightarrow H + H + H \tag{R13}$$

and

$$H_3^+ + e \rightarrow H_2 + H \tag{R14}$$

leading back to H or H_2.

Cosmic-ray ionization [R8], and cosmic-ray dissociation

$$H_2 + cr \rightarrow H + H \tag{R15}$$

are the main H_2 removal mechanisms at cloud depths that are fully shielded from photodissociating far-UV radiation. Dissociative ionization

$$H_2 + cr \rightarrow H + H^+ + e \tag{R16}$$

is an additional (minor) removal channel. As we discuss further in our analysis below (§3), when the ionization, [R8], is followed by an abstraction, [R10], an additional H_2 molecule is removed for every H_3^+ ion that dissociatively recombines into three atoms, [R13].

A primary H_2 destruction process is photodissociation by 912-1108 Å Lyman-Werner (LW) photons

$$H_2 + \nu_{LW} \rightarrow H + H \quad , \tag{R17}$$

in the $B^1\Sigma_u - X^1\Sigma_g^+$ and $C^1\Pi_u - X^1\Sigma_g^+$ absorption line systems. Photodissociation is generally the dominant H_2 removal mechanism unless self-shielding is very significant, as we discuss in §3 and §4. (We are neglecting dust absorption.) We assume that any hydrogen ionizing ultraviolet (EUV) radiation is absorbed outside the predominantly neutral atomic/molecular medium we are studying. Furthermore, we do not consider penetrating X-rays here. Local X-ray ionization is similar in its effects to cosmic-ray ionization. For simplicity of following the ionization driven chemistry, we assume that the ionization is provided by just cosmic-ray impacts throughout.

In sufficiently dense gas, H_2 is also produced by the three-body reaction

$$H + H + H \rightarrow H_2 + H \quad . \tag{R18}$$

However, this requires very dense gas $\gtrsim 10^8$ cm^{-3}, as may occur in collapsing clouds (Palla et al. 1983; Abel et al. 2002; Turk et al. 2012) and we do not consider this regime here. H_2 is also removed by collisional dissociation

$$H + H_2 \rightarrow H + H + H \quad , \tag{R19}$$

however, this requires warm gas, with $T \gtrsim 1000$ K (Martin et al. 1996), which is also outside our modeling regime that we are restricting to cool/cold gas.

2.1.2. *Helium Network*

For completeness we include the metals-free helium chemistry. Helium atoms are ionized by cosmic-ray impact

$$He + cr \rightarrow He^+ + e \quad , \tag{R20}$$

and neutralization is by rapid charge transfer and dissociative charge transfer

$$He^+ + H \rightarrow He + H^+ \tag{R21}$$

$$He^+ + H_2 \rightarrow He + H_2^+ \tag{R22}$$

$$He^+ + H_2 \rightarrow He + H + H^+ \quad . \tag{R23}$$

Radiative recombination

$$He^+ + e \rightarrow He + \nu \tag{R24}$$

is an additional minor removal channel.

In cold predominantly neutral gas, the molecular ion HeH^+ is produced by the radiative associations

$$H + He^+ \rightarrow HeH^+ + \nu \tag{R25}$$

$$H^+ + He \rightarrow HeH^+ + \nu \quad , \tag{R26}$$

and is removed by

$$HeH^+ + H \rightarrow He + H_2^+, \tag{R27}$$

$$HeH^+ + H_2 \rightarrow He + H_3^+ \quad . \tag{R28}$$

In our models dissociative recombination

$$HeH^+ + e \rightarrow He + H \tag{R29}$$

is a very minor removal channel because the electron fractions remain low. Photodissociation

$$HeH^+ + \nu \rightarrow He + H^+ \tag{R30}$$

is also a minor removal channel in our parameter space.

Reactions [R25] and [R26] [5] followed by [R27] and [R6], as well as [R5] followed by [R6], were primary sources of H_2 following cosmic recombination and prior to the introduction of the first reionization sources. At redshifts $z \gtrsim 100$, and at the prevailing mean gas densities, any H^- produced via relic electrons ions were rapidly photodetached by thermal background photons (Lepp et al. 2002; Galli & Palla 2013). In the computations we consider here, we assume efficient formation of H^- via free electrons produced by local sources of ionizing cosmic-rays, and the H_2 is formed mainly by [R1] and [R2]. The main parameters controlling the chemistry are the Lyman-Werner radiation intensity and associated photodissociation rate, the cosmic-ray ionization rate, the gas density, and the cloud temperature. We assume that photodetachment is by the same radiation source that also photodissociates the H_2. For our parameter space, and relatively dense gas conditions, photodetachment is therefore negligible, and our results are insensitive to the IR to UV spectral shapes as we discuss below.

2.2. *FUV radiation*

In our study we compute depth dependent HI and H_2 density profiles for dust-free clouds exposed to fluxes of far-UV photons and cosmic-ray particles. We determine conditions for which an HI-to-H_2 transition occurs assuming steady-state conditions.

2.2.1. *Radiation Spectra*

We parameterize the far-UV radiation flux, in particular the dissociating Lyman-Werner band flux, relative to the standard Draine (1978) Galactic FUV interstellar field strength (Parravano et al. 2003; Bialy 2020).

For the Draine far-UV spectrum, the flux in the (narrow) 912-1108 Å LW band is $F_{LW} = 2.07 \times 10^7 I_{LW}$ photons cm^{-2} s^{-1}. I_{LW} is the radiation field strength[6] relative to the free-space unattenuated Draine field in the LW band, for which $I_{LW} = 1$. The unattenuated H_2 photodissociation rate due to absorptions in all of the LW lines is $D_0 = \sigma_d \bar{F}_{\nu,LW} = 5.8 \times 10^{-11}$ s$^{-1} I_{LW}$. Here $\bar{F}_{\nu,LW}$ is the mean flux-density (photons cm^{-2} s^{-1} Hz^{-1}) in the LW band, and $\sigma_d = 2.36 \times 10^{-3}$ cm^2 Hz is the total H_2-line photodissociation cross section, summed over all the LW absorption lines (see S14). For the Draine spectrum, the H^- photodetachment rate is $D_- = 5.6 \times 10^{-9} I_{LW}$ s^{-1}, and $D_-/D_0 = 96.6$. We computed the photodetachment rate using the Miyake et al.

[5] Reaction [R25] dominates the formation of HeH^+ in the partially ionized interface zones in planetary nebulae where removal by [R29] is important in addition to [R27]. Interstellar HeH^+ was recently observed for the first time in the planetary nebula NGC7027 (Güsten et al. 2019; Neufeld et al. 2020). In such nebulae, associative ionization $H + He(2^3S) \rightarrow HeH^+ + e$ involving the metastable helium produced via recombination, is also an important source of HeH^+ (Roberge & Dalgarno 1982; Neufeld et al. 2020).

[6] In S14 we refer to the intensity parameter as I_{UV}, and normalize to the entire 6-13.6 eV FUV band. Here we use the subscript "LW" to emphasize normalization relative to just the Lyman-Werner band.

(2010) cross section (see their Fig. 1) and integrating from the infrared threshold (1.6 μm) to the Lyman limit (912 Å).

More generally, the ratio D_-/D_0 depends on the shape of the radiation spectrum from the near-IR to the UV (Wolcott-Green et al. 2017). In Figure 2 we plot four radiation spectra, for pure Draine, combination Draine+MathisIR (Mathis et al. 1983), and 10^4 and 10^5 K blackbody fields[7]. We normalize the spectra in Figure 2 such that they all have the same flux of 2.07×10^7 photons cm^{-2} s^{-1} in the LW band, appropriate for $I_{\rm LW} = 1$. In Table 3 we list J_{21} for these fields, defined as the flux densities at the Lyman limit in units of 10^{-21} erg cm^2 s^{-1} Hz^{-1} sr^{-1}.

Because the LW band is narrow, we make the simplifying approximation that for equal LW fluxes the unattenuated H_2 dissociation rate is independent of the spectral shape and equal to $D_0 = 5.8 \times 10^{-11} I_{\rm LW}$ s^{-1}. However, the H^- photodetachement rate is very sensitive to the spectral shape. In Table 3 we list D_- and D_-/D_0 for the four radiation fields. In Figure 3 we plot these quantities as functions of the radiation temperature, $T_{\rm rad}$, for pure blackbody fields, all normalized such that $I_{rmLW} = 1$ at any Trad. Figure 3 shows that D_-/D_0 grows rapidly for $T_{\rm rad}$ below $\sim 2 \times 10^4$ K. In the computations in this paper we assume 10^5 K spectra, appropriate for massive pop III stars, for which $D_- = 2.7 \times 10^{-9} I_{\rm LW}$ s^{-1}, and $D_-/D_0 = 46.5$. But even for this large ratio photodetachment does not play a role in our model parameter space, as we discuss further below.

For reference, in Figure 2 we also plot the expected cosmological metagalactic radiation spectra (unnormalized) computed by Haardt & Madau (2012), at redshifts z=0.05, 1.05, and 5.18. In Table 4 we list J_{21}, $I_{\rm LW}$, D_-, and D_-/D_0, for these three cosmological radiation fields.

2.2.2. *Shielding*

We are considering dust-free gas for which any attenuation of the H_2 photodissociation rate is due entirely to self-shielding optical depth in the H_2 absorption lines. In the dust-free regime the photodissociation rate at any depth into a semi-infinite plane-parallel slab is

$$D(N) = \frac{1}{2} D_0 f_{\rm shield}(N_{\rm H_2}) \quad . \tag{1}$$

Here, $N = N_{\rm HI} + 2N_{\rm H_2}$ is the total column density of hydrogen nuclei, atomic (HI) plus molecular (H_2), from the surface to a depth, z (cm), in the cloud. The factor of 1/2 accounts for reduction of the rate relative to free-space by the cloud itself, with radiation incident from one hemisphere only, and opaque to any radiation from the other side. This is the "semi-infinite" limit. In this paper we assume beamed fields with incident rays all normal to the cloud surface[8].

The H_2 self-shielding function is defined by

$$f_{\rm shield}(N_{\rm H_2}) \equiv \frac{1}{\sigma_d} \frac{dW_d(N_{\rm H_2})}{dN_{\rm H_2}} \quad . \tag{2}$$

[7] Mathis et al. (1983) represented their inferred IR Galactic stellar spectrum as a sum of diluted blackbodies at 3000, 4000, and 7500K, representing the late-type stars. The Draine (1978) field is due primarily to the early OB type stars.

[8] See S14 for a discussion of beamed versus isotropic irradiation.

In this expression, $W_d(N_{\rm H_2})$ is the bandwidth (Hz) of LW radiation absorbed in photodissociations, through all of the absorption lines, up to a molecular column $N_{\rm H_2}$ in a dust-free cloud, and σ_d is the total H_2-line photodissociation cross section. For cool ($\lesssim 500$ K) gas the self-shielding function is well-approximated by (Draine & Bertoldi 1996, S14)

$$f_{\rm shield} = \frac{0.965}{(1+x/b_5)^2} + \frac{0.035}{(1+x)^{0.5}} \times \exp[-8.5 \times 10^{-4}(1+x)^{0.5}] \tag{3}$$

where $x \equiv N_{\rm H_2}/(5 \times 10^{14}$ cm$^{-2})$ and $b_5 \equiv b/(10^5$cm s$^{-1})$ is the normalized absorption-line Doppler parameter. Alternate expressions have also been presented, especially for warmer material (e.g., Wolcott-Green et al. 2011). Here we adopt Eq. (3).

For very small H_2 column density, $f_{\rm shield} = 1$. The onset of self-shielding occurs for $N_{\rm H_2} \sim 10^{14}$ cm^{-2}, depending on b (we set $b_5 = 2$). As discussed by Bialy & Sternberg (2016, see their Fig. is 5), the atomic-to-molecular transition points are insensitive to the Doppler widths. For $N_{\rm H_2} \gtrsim 10^{17}$ cm^{-2} the absorptions occur out of the line damping wings and $f_{\rm shield}$ becomes small, decreasing to $\sim 10^{-5}$ for $N_{\rm H_2} \sim 10^{21}$ cm^{-2} and the dissociation rate is very significantly reduced. For $N_{\rm H_2} \gtrsim 10^{22}$ cm^{-2} the absorption lines overlap and the LW band is completely blocked (Draine & Bertoldi 1996; Sternberg et al. 2014). In this limit, $f_{\rm shield} \to 0$ and the photodissociation rate becomes vanishingly small. Self-shielding including line overlap[9] enables an HI-to-H_2 transition even in the absence of dust shielding as we discuss below.

The dissociation bandwidth in Eq. (2) is given by the fit formula[10] (Bialy & Sternberg 2016),

$$W_d(N_{\rm H_2}) = a_1 \ln\left[\frac{a_2 + y}{1 + y/a_3}\right] \left(\frac{1+y/a_3}{1+y/a_4}\right)^{0.4} , \tag{4}$$

where

$$\begin{aligned} y &\equiv \frac{N_{\rm H_2}}{10^{14}\ {\rm cm}^{-2}} \\ a_1 &= 3.6 \times 10^{11}\ {\rm Hz} \\ a_2 &= 0.62 \\ a_3 &= 2.6 \times 10^3 \\ a_4 &= 1.4 \times 10^7 \quad . \end{aligned}$$

Equation (4) is valid for $y \geq 1$. For complete line absorption of the dissociating radiation in the LW band, $W_{\rm d,tot} = 8.8 \times 10^{13}$ Hz, and the total dissociation flux absorbed in an optically thick cloud is $\bar{F}_\nu W_{\rm d,tot} = 2.2 \times 10^6 I_{\rm LW}$ photons cm^{-2} s^{-1}. This is 10% of the total LW

[9] Line overlap occurs when the dust abundance and associated continuum opacity are small enough such that LW photons are absorbed in the outer Lorentzian damping wings of adjacent lines, prior to any dust absorption. This generally requires a LW dust-grain absorption cross section per hydrogen nucleus $\sigma_g \lesssim 10^{-22}$ cm^{-2}, for which the associated dust opacity $2\sigma_g N_{\rm H_2} \lesssim 1$.

[10] In Bialy & Sternberg (2016) our expression for the H_2 dissociation bandwidth also includes a dependence on the assumed dust absorption cross section. Here we are assuming $\sigma_g = 0$.

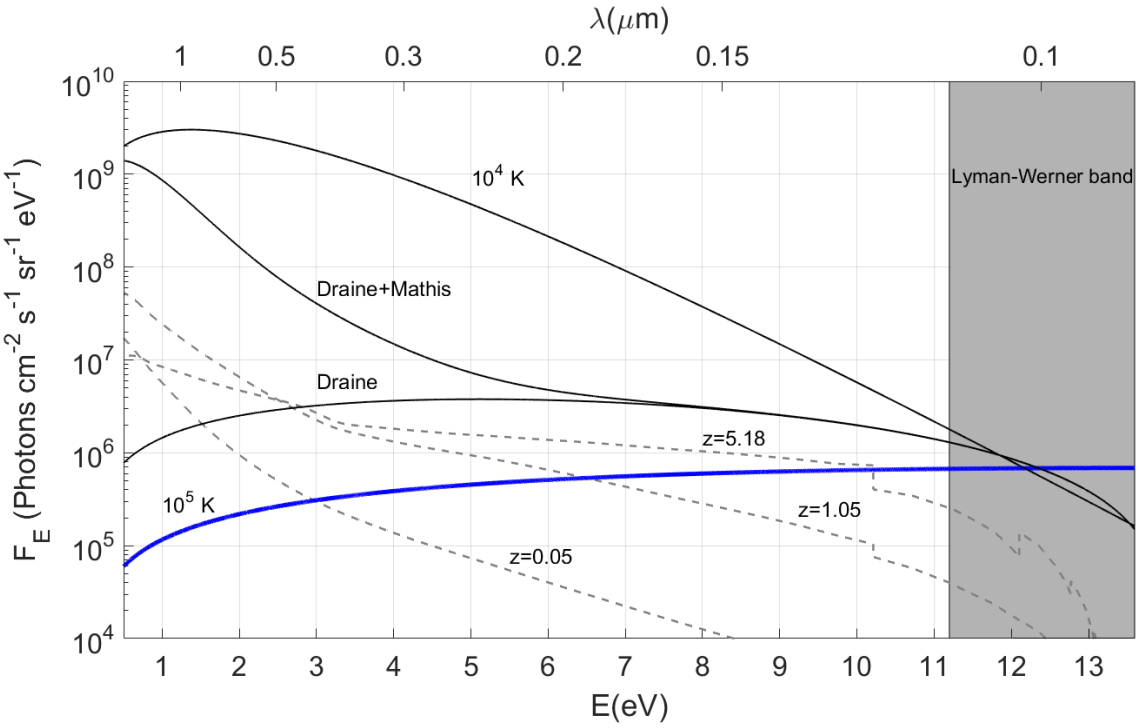


FIG. 2.— Solid curves show the (normalized) stellar-based radiation fields, Draine, Draine+Mathis, and 10^4 and 10^5 K blackbody spectra, all normalized such that $I_{\rm LW} = 1$ in the Lyman-Werner band (shaded region). The dashed curves are the absolute (unnormalized) Haardt & Madau (2012) metagalactic background radiation fields from low- to high redshift.

TABLE 3
PHOTO-RATES FOR STELLAR-BASED RADIATION FIELDS

Stellar Based	J_{21} [a]	$D_-(\mathrm{s}^{-1})$ [b]	D_-/D_0 [c]	$(I_{LW}/n_6)_{\rm crit}$ [d]
Draine	13.5	5.58×10^{-9}	96.6	7.28×10^5
Draine+Mathis	13.5	2.73×10^{-7}	4.66×10^3	6.88×10^3
10^4 K	14.6	1.77×10^{-7}	3.05×10^3	1.14×10^4
10^5 K	61.8	2.77×10^{-9}	47.8	1.56×10^6

[a] The radiation flux densities at the Lyman limit, in units of 10^{-21} ergs s^{-1} cm^{-2} Hz^{-1} sr^{-1}, assuming each field is normalized to $I_{\rm LW} = 1$.
[b] The H^- photodetachment rates for the normalized fields.
[c] The ratio D_-/D_0 of the H^- photodetachment rate and H_2 photodissociation rate.
[d] The critical ratios $(I_{\rm LW}/n_6)_{\rm crit}$ above which photodetachment reduces the H^- abundance (see text).

TABLE 4
PHOTO-RATES FOR METAGALACTIC FIELDS

Metagalactic	J_{21} [a]	$I_{\rm LW}$ [b]	$D_-(\mathrm{s}^{-1})$ [c]	D_-/D_0 [d]	$(n_6)_{\rm crit}$ [e]	$(n/n_b)_{\rm crit}$ [f]
$z = 0.05$	8.24×10^{-3}	7.00×10^{-4}	1.70×10^{-9}	4.19×10^4	3.9×10^{-7}	1.36×10^6
$z = 1.05$	0.141	2.67×10^{-2}	9.54×10^{-9}	8.37×10^3	2.72×10^{-6}	1.27×10^6
$z = 5.18$	0.188	1.26×10^{-1}	6.16×10^{-9}	8.44×10^2	1.61×10^{-6}	2.75×10^4

[a] Flux density J_{21} at the Lyman limit.
[b] LW intensity.
[c] H^- photodetachment rate.
[d] The ratio D_-/D_0 of the H^- photodetachment rate and H_2 photodissociation rate.
[e] The critical density $n_{6,\rm crit}$ below which photodetachment reduces the H^- abundance (see text).
[f] The critical photodetachment density relative to the mean cosmic baryon density $n_b = 2.48 \times 10^{-7}(1+z)^3$ cm^{-3}.

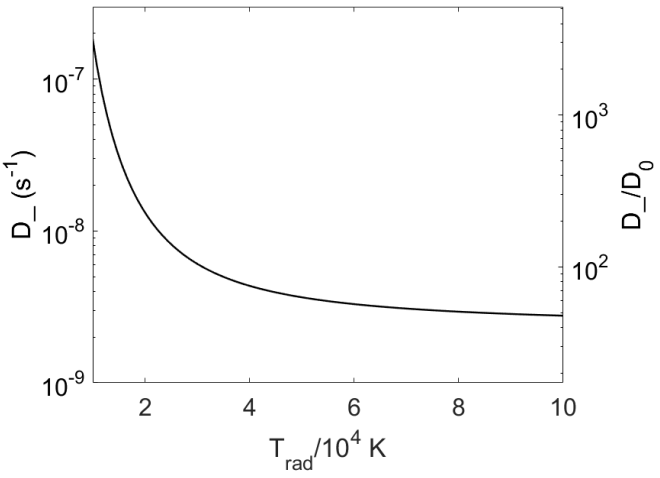


FIG. 3.— The H^- photodetachment rate (left axis) and ratio of the H^- photodetachment and H_2 photodissociation rates (right axis) as functions of radiation temperature for black body spectra, normalized to $I_{\rm LW} = 1$ for any $T_{\rm rad}$.

flux, and is reradiated as dissociation continuum. The remaining energy is reradiated as Lyman-Werner band emission lines (Sternberg 1989) terminating in mainly excited vibrational levels of the ground electronic state.

2.3. *Cosmic Rays*

Low level ionization in the shielded ISM of galaxies is generally maintained by low-energy cosmic rays. (Spitzer & Tomasko 1968; Dalgarno 2006). In localized environments photoionization by penetrating X-rays may also contribute in addition to the cosmic-ray impacts. Within molecular clouds cosmic-ray ionization drives a rich ion-molecule chemistry, and controls the dynamical coupling of magnetic fields to the gas. In the Milky Way, the characteristic H_2 cosmic-ray ionization rate is $\sim 10^{-16}$ s^{-1}, although the rates may vary with location in the Galaxy and with cloud depth. (Padovani et al. 2009; Neufeld & Wolfire 2017). The cosmic-ray fluxes and ionization rates may be substantially larger in galaxies with elevated star-formation activity and FUV fields (Mashian et al. 2013; Bialy & Sternberg 2015; Bisbas et al. 2017; Bialy 2020).

Our parameter ζ is the total cosmic-ray H_2 ionization rate (s^{-1}) due to non-dissociative ([R8]) plus dissociative ([R15]) ionizations. We define the normalized rate $\zeta_{-16} \equiv \zeta/(10^{-16}$ s$^{-1})$. The relative rates of all of the cosmic-ray ionization and dissociation processes in our network are listed in Table 2. An important parameter for the chemistry is the number of H_2 dissociations per CR ionization, including the effects of the secondary electrons for both processes (Cravens & Dalgarno 1978; Li & Goldsmith 2003; Goldsmith & Li 2005). Following Padovani et al. (2018a) we assume 0.7 dissociations per ionization. This is the asymptotic ratio for large penetration depths.

The penetration and transport of cosmic-rays, and the possible attenuation of the associated ionization rates with cloud depth, depend on a wide range of (uncertain) properties including the spectrum of the low energy particles, the distributions and orientations of the magnetic fields, the particle gyroradii, free-streaming ionization energy losses, particle production, and the characteristics of MHD turbulent diffusion (Ivlev et al. 2018; Padovani et al. 2020).

We therefore construct two families of models for (a) constant ionization rates through the clouds, and (b) attenuation of the ionization rates assuming a power-law form for the energy losses. For model family (b), we adopt the Padovani et al. (2018b) results for the particle energy losses and transport for the "Voyager-1 based" cosmic-ray input spectrum (Cummings et al. 2016). The Padovani et al. (2018b) CR ionization rates, for low- and high-ionization cosmic-ray spectra (their models $\mathcal{L}$ and $\mathcal{H}$), may be expressed as simple power-laws

$$\zeta = \zeta_0 \times \left(\frac{N_{\rm eff}}{10^{19}\ {\rm cm}^{-2}} \right)^{-q} \quad , \tag{5}$$

where $N_{\rm eff}$ is the effective cosmic-ray absorbing gas column. The effective column depends on the orientation angle θ of the magnetic field along which the cosmic-ray protons propagate relative to the cloud normal, so that $N_{\rm eff} = N/\mu$, where $\mu \equiv cos\theta$. Equation (5) is valid for $N_{\rm eff}$ between 10^{19} and 10^{24} cm^{-2}, the relevant range for our considerations. We find that $q = 0.280$ and $q = 0.385$ for the Padovani models $\mathcal{L}$ and $\mathcal{H}$ respectively, with an accuracy of 37% and 6%. For $N_{\rm eff} < 10^{19}$ cm^{-2} we assume $\zeta = \zeta_0$.

3. ANALYSIS

In §4 we present our numerical solutions to the chemical rate equations and resulting HI/H_2 density profiles, including computations of the atomic to molecular transition points, for the dust-free conditions we are considering. Before presenting our numerical calculations we first provide an analytic description as a guide.

3.1. *HI/H_2 Balance*

In a steady state, we write the H_2 formation-destruction equation as

$$R_- n x_{\rm HI} = \left\{ \frac{1}{2} D_0 f_{\rm shield}(N_{\rm H_2}) + [0.96 f_d (1+f_3) + 0.7 + 0.04]\zeta \right\} x_{\rm H_2} \tag{6}$$

In this expression, $x_{\rm HI} \equiv n_{\rm HI}/n$ and $x_{\rm H_2} \equiv n_{\rm H_2}/n$ are the depth dependent atomic (HI) and molecular (H_2) abundance fractions, and $n = n_{\rm HI} + 2n_{\rm H_2}$ is the total hydrogen volume density. We are assuming that the additional constituents all have very low abundances compared to HI or H_2. On the left-hand side, R_- is the effective rate coefficient for H_2 formation via the H^- sequence, [R1] and [R2] (Bialy & Sternberg 2019). The first term on the right-hand side is the depth dependent photodissociation rate in the photodissociation region (PDR). It vanishes in the inner cosmic-ray zone (CRZ) where cosmic-ray ionization and dissociation become the main H_2 removal mechanisms. These are included in the second term in brackets multiplied by ζ. The numerical factors are the relative rates for [R8], [R14], and [R15] respectively (see Table 2).

In Eq.(6), the factor 0.96ζ for cosmic-ray ionization is multiplied by the branching ratio

$$f_d = \frac{k_{10} x_{\rm H_2}}{k_{10} x_{\rm H_2} + k_6 x_{\rm HI}} \quad . \tag{7}$$

This is the probability that the production of H_2^+ via ionization is followed by the abstraction reaction [R10]

to H_3^+ rather than charge transfer [R6] back to H_2 (see Eq 15 in Bialy & Sternberg 2015). Dissociative recombination of H_2^+ [R11] may be ignored because the fractional ionizations are small. The additional factor

$$1 + f_3 = 1 + \frac{k_{13}}{k_{13} + k_{14}} \quad , \tag{8}$$

where $f_3 = 0.65$ is the branching ratio for dissociative recombination fragmentation of H_3^+ into three atoms, [R13], rather than back to H_2, [R14] (see Fig. 1). The product, $(1 + f_3)f_d$ is then the net number of H_2 molecules removed per ionization event [R8]. This number is depth dependent because f_d depends on the atomic and molecular factions, $x_{\rm HI}$ and $x_{\rm H_2}$. Thus, for $x_{\rm HI} \approx 1$, e.g. in photodissociated gas, $f_d = 0$ and cosmic-ray ionization [R8] is ineffective in further reducing the small molecular fraction. For $x_{\rm H_2} \approx 0.5$, the branching ratio $f_d = 1$, and 1.65 hydrogen molecules are removed per cosmic-ray ionization event. Cosmic-ray dissociation [R15] remains operative throughout. It is important in the CRZ, but is a minor H_2 removal process in the PDR.

Following Bialy & Sternberg (2019) we write

$$R_- = \eta k_1 x_{\rm e} \tag{9}$$

where $x_{\rm e} \equiv n_e/n$ is the electron fraction, and k_1 is the rate coefficient of the radiative attachment reaction [R1]. The branching ratio

$$\eta = \frac{k_2 x_{\rm HI}}{k_2 x_{\rm HI} + k_3 x_{\rm H^+} + D_-/n} \tag{10}$$

is the fraction of radiative attachments that are followed by associative detachment [R2] rather than mutual neutralization [R3] or photodetachment [R4]. For $\eta = 1$ all radiative attachments result in H_2 formation.

Throughout the PDR and into the CRZ, including where the gas is molecular, the electron and proton fractions are equal, i.e. the positive charge is carried mainly by protons. This is because the positive molecular ions produced by CR ionization of H_2 [R8] are rapidly removed by abstraction [R10], followed by rapid dissociative recombination [R13], and [R14]. The fraction of H_2 ionizations leading to H^+ [R15] is small, and CR ionization of atomic hydrogen [R7] is the dominant source of electrons throughout. With the further assumption that the gas is neutral, i.e. $x_{\rm e} \ll 1$, (and with the neglect of helium ionization), we have that

$$x_{\rm e} = \left(\frac{0.46\zeta}{n\alpha_{\rm B}} x_{\rm HI}\right)^{1/2} = 2.4\times10^{-6}\left(\frac{\zeta_{-16}}{n_6}\right)^{1/2} T_2^{3/8} x_{\rm HI}^{1/2} \quad , \tag{11}$$

where $\alpha_{\rm B}$ is the electron-proton recombinaton rate coefficient, $n_6 = n/(10^6\ {\rm cm}^3)$, and $T_2 = T/100{\rm K}$. In this approximation, $x_{\rm H^+} = x_{\rm e}$.

The branching ratio η becomes small ($\lesssim 0.5$) if the proton fraction $x_{\rm H^+} \gtrsim (k_2/k_3)x_{\rm HI}$, or if $D_- \gtrsim k_2 n x_{\rm HI}$. For atomic gas ($x_{\rm HI} = 1$), $\eta < 0.5$ for $x_{\rm H^+} > 0.03$. This requires $\zeta_{-16}/n_6 > 2.21\times10^8$ as given by Eq.(11) (for $T = 100$ K). For the $T = 10^5$ K spectrum we assume in our computations, $\eta < 0.5$ and photodetachment becomes important for $I_{\rm LW}/n_6 > (I_{\rm LW}/n_6)_{\rm crit} = 1.6\times10^6$. In Table 3 we list the critical UV-intensity to density ratios, $(I_{\rm LW}/n_6)_{\rm crit}$, at which $\eta = 0.5$ for the different spectral shapes.

For comparison, in Table 4 we give the critical densities, $n_{6,crit}$, below which H^- photodetachment becomes important for the (unnormalized) metagalactic fields at the various redshifts. We also list these densities relative to the cosmic mean baryon densities n_b at the different epochs. Relative to the cosmic mean densities, photodetachment by the evolving metagalactic field is more effective at lower redshift.

For the parameter space we are considering it is safe to assume $\eta = 1$, and we then have

$$R_- = 4\times10^{-22}\left(\frac{\zeta_{-16}}{n_6}\right)^{1/2} T_2^{1.02} e^{-0.09/T_2} x_{\rm HI}^{1/2} \ \ {\rm cm^3\ s^{-1}} \quad . \tag{12}$$

Equation (11) is valid for ζ_{-16}/n_6 up to $\sim 1.7\times10^9$ for which $x_{\rm e} \lesssim 0.1$ (for $x_{\rm HI} = 1$). For this maximal ionization fraction (with the gas still mainly neutral) $R_- \approx 1.6\times10^{-17}$ cm^3 s^{-1} at 100 K. Remarkably, this is comparable to the characteristic $R_{\rm dust} = 3\times10^{-17}$ cm^3 s^{-1} for grain-surface catalysis of H_2 for typical Galactic dust-to-gas ratios, $Z'_d = 1$. However, for $\zeta_{-16} = 1$ this requires extremely low density $n_6 \sim 6\times10^{-10}$ ($n = 6\times10^{-4}$ cm^{-3}). In general, $R_- \ll R_{\rm dust}$ for typical ISM conditions. For $\zeta_{-16} = n_6 = 1$, $R_- = 3.65\times10^{-22}$ cm^3 s^{-1} at 100 K (for $x_{\rm HI} = 1$), and gas-phase formation becomes important for very small dust-to-gas ratios $Z'_d \lesssim 1.3\times10^{-5}(\zeta_{-16}/n_6)^{1/2}$. However, such low dust-to-gas ratios may not require correspondingly small metallicities because the dust abundances may decline sharply and non-linearly. For example, given the Rémy-Ruyer et al. (2013) broken power-law representation for the gas-to-dust ratio, Z'_d, versus overerall metallicity, Z', into the low metallicity regime (see also Bialy & Sternberg 2019; Li et al. 2019), gas phase H_2 formation dominates for $Z' \lesssim 0.01(\zeta_{-16}/n_6)^{1/6}$ at 100 K. Furthermore, R_- increases with temperature, whereas $R_{\rm dust}$ probably declines (Cuppen et al. 2010), so the relative efficiencies of the gas-phase processes may grow in warmer gas (Glover 2003).

In dusty clouds, electrons are provided by the photoionization of heavy elements, and dust neutralization processes may reduce the ionization fractions. As we discuss in Appendix A, heavy element ionization is negligible for $Z' \lesssim 0.01(\zeta_{-16}/n_6)^{1/2}$, and dust grain neutralization is unimportant for $Z'_d \lesssim 10^{-5}$. Coincidentally, this is the gas-to-dust ratio for which H_2 formation on dust may be ignored as well.

Because R_- is proportional to $(\zeta/n)^{1/2}$, whereas destruction is proportional to (ζ/n), the molecular fraction *decreases* with ζ/n in the CRZ as we discuss further below. For any ζ, the effective rate coefficient $R_- \propto n^{-1/2}$, due to the lower electron fractions at larger densities. The *rate* of gas phase H_2 formation, $R_- n$ (s^{-1}), is therefore proportional to $n^{1/2}$.

Equation (11) may also be used to estimate the H^- abundance. Assuming formation via [R1] and removal by just [R2] we obtain the upper limit

$$x_{H^-} \lesssim \frac{k_1}{k_2} x_{\rm e} = 6.04\times10^{-14} T_2^{1.41} e^{0.3/T_2} \left(\frac{\zeta_{-16}}{n_6}\right)^{1/2} x_{\rm HI}^{1/2} \quad . \tag{13}$$

Although the H^- anions are critical intermediaries for H_2 formation, their abundance remains extremely small for steady-state conditions.

3.2. *PDR*

In the PDR, Eq.(6) may be written as

$$x_{\rm HI} = \frac{1}{2}\alpha f_{\rm shield}(N_{\rm H_2})x_{\rm H_2} \tag{14}$$

where

$$\alpha \equiv \frac{D_0}{R_- n} = \frac{\sigma_d \bar{F}_{\nu,\rm LW}}{R_- n} \tag{15}$$
$$= 1.45\times10^5\big(\frac{I_{\rm LW}}{n_6}\big)\big(\frac{\zeta_{-16}}{n_6}\big)^{-1/2}T_2^{-1.02}x_{\rm HI}^{-1/2} \quad .$$

The unattenuated photodissociation rate, D_0, depends on the far-UV field strength, $I_{\rm LW}$, so the dimensionless parameter α is a function of the two ratios $I_{\rm LW}/n$ and ζ/n (via R_-). In general the gas is atomic ($x_{\rm HI}=1$) at the unshielded cloud boundary, and the H_2 fraction is

$$x_{\rm H_2} = \frac{2}{\alpha} = 1.38\times10^{-5}\big(\frac{I_{\rm LW}}{n_6}\big)^{-1}\big(\frac{\zeta_{-16}}{n_6}\big)^{1/2} \quad . \tag{16}$$

For fiducial parameters, $I_{\rm LW}=\zeta_{-16}=n_6=1$, the molecular fraction $x_{\rm H_2}=1.38\times10^{-5}$ at the cloud boundary, and a molecular self-shielding column of $\gtrsim 10^{21}$ cm^{-2} for which $f_{\rm shield}\lesssim 10^{-5}$ is required to enable an HI-to-H_2 transition.

Equation (14) may be written as the differential equation

$$dN_{\rm HI} = \frac{1}{2}\alpha f_{\rm shield}(N_{\rm H_2})dN_{\rm H_2} \tag{17}$$

for the HI column as a function of the H_2 column. For a constant α, independent of cloud depth, integrating gives

$$N_{\rm HI}(N_{\rm H_2}) = \frac{\alpha}{2}\int_0^{N_{\rm H_2}} f_{\rm shield}(N'_{\rm H_2})dN'_{\rm H_2} = \alpha\frac{W_d(N_{\rm H_2})}{\sigma_d} \quad , \tag{18}$$

where σ_d is the line dissociation cross section (cm^2 Hz), and $W_d(N_{\rm H_2})$ is the dissociation bandwidth, as given by Equation (4). In pulling α out of the integral we are assuming (a) constant gas density for the given $I_{\rm LW}$ and ζ_{-16}, (b) that $x_{\rm HI}^{1/2}\approx 1$, i.e. the gas is largely atomic, where photodissociation dominates the production of the HI column, and (c) no CR attenuation so that ζ_{-16} is constant. Equation (18) can also be written as

$$N_{\rm HI}(N_{\rm H_2}) = \frac{1}{2}\frac{\bar{F}_{\nu,\rm LW}W_d(N_{\rm H_2})}{R_- n} \quad . \tag{19}$$

The numerator, $\bar{F}_{\nu,\rm LW}W_d(N_{\rm H_2})/2$, is the radiation flux absorbed in dissociations up to a molecular column $N_{\rm H_2}$, and this is equal to the product $R_- n N_{\rm HI}(N_{\rm H_2})$, i.e. the rate at which molecules are produced within $N_{\rm H_2}$.

For sufficiently large $N_{\rm H_2}$ ($\gtrsim 10^{22}$ cm^{-2}) the H_2 absorption lines fully overlap, and all of the LW band photons are absorbed by the H_2. The total HI column maintained by photodissociation by LW band photons is then

$$N^{\rm LW}_{\rm HI,tot} = \frac{\alpha}{2}\frac{W_{d,\rm tot}}{\sigma_d} = \frac{1}{2}\frac{\bar{F}_{\nu,\rm LW}W_{d,\rm tot}}{R_- n} \tag{20}$$
$$= 2.7\times10^{21}\big(\frac{I_{\rm LW}}{n_6}\big)\big(\frac{\zeta_{-16}}{n_6}\big)^{-0.5} \quad \rm cm^{-2} \quad .$$

In the third equality we have set $T_2=1$, and $x_{\rm HI}=1$ in the expression for R_- with the assumption that the photodissociated HI is built up in an extended fully atomic PDR and the transition from HI to H_2 is sharp. This assumption is valid if the transition occurs as the absorption lines overlap, in which case the dissociation rates are reduced exponentially leading to sharp transitions. Setting $x_{\rm HI}=1$ is more approximate when the transition points occur before the lines overlap in which case further LW absorptions out of the damping wings enable continued gradual growth of the photodissociated HI columns in the molecular zones. Sharp transitions induced by line-overlap occur when $N^{\rm LW}_{\rm HI,tot}\gtrsim 10^{22}$ cm^{-2}.

We select fiducial parameters, $I_{\rm LW}=\zeta_{-16}=n_6=1$ (or $I_{\rm LW}/n_6=\zeta_{-16}/n_6=1$) such that the resulting HI photodissociation column, $N^{\rm LW}_{\rm HI,tot}=2.7\times10^{21}$ cm^{-2}, is comparable to the H_2 shielding column $\sim 10^{22}$ required for line overlap.

It is of interest to compare Eq. (20) to the S14 formula for the total HI photodissociation column in dusty clouds, where molecule formation is via grain catalysis, and opacity is provided by FUV dust absorption in addition to H_2 self-shielding. The S14 formula (for beamed fields) is

$$N^{\rm LW}_{\rm HI,tot} = \frac{1}{\sigma_g}\ln\big[\frac{1}{2}\frac{\sigma_g\bar{F}_\nu W_{g,\rm tot}}{R_{\rm dust}n}+1\big] \quad , \tag{21}$$

where σ_g is the dust absorption cross section, $R_{\rm dust}$ is the grain-surface H_2 formation rate coefficient, and $W_{g,\rm tot}$ is the "H_2 dust limited dissociation bandwidth" (see S14). For vanishing dust abundance, $\sigma_g\rightarrow 0$, $W_{g,\rm tot}\rightarrow W_{d,\rm tot}$, and $R_{\rm dust}$ may be replaced with the gas-phase coefficient R_-. Expanding the logarithm, σ_g cancels out, and this yields our Eq.(20) for dust-free conditions. We further discuss Eq. (20) versus (21) in Appendix B.

3.3. *CRZ*

The transition from the outer PDR to the inner cosmic-ray zone (CRZ) occurs as self-shielding reduces the H_2 photodissociation rate below the CR destruction rate. In the CRZ, H_2 formation continues to be driven by CR ionization. Removal is by a combination of CR ionization and dissociation.

Moving from the PDR to CRZ may, or may not, give rise to an atomic to molecular transition, depending on ζ/n, as follows. In the CRZ, Eq.(6) may be written as

$$R_- n x_{\rm HI} = [0.96 f_d(1+f_3)+0.74]\zeta x_{\rm H_2} \quad . \tag{22}$$

In analogy to Eq.(14) for the PDR, this may be written as

$$x_{\rm HI} = \beta x_{\rm H_2} \tag{23}$$

where implicitly

$$\beta \equiv [0.96 f_d(1+f_3)+0.74]\frac{\zeta}{R_- n} \quad (24)$$
$$= [0.96(1+f_3)\frac{1}{1+k_6 x_{\rm HI}/k_{10}x_{\rm H_2}}+0.74]\frac{\zeta}{R_- n}$$
$$= 0.25\times[\frac{1.58}{1+0.31 x_{\rm HI}/x_{\rm H_2}}+0.74](\frac{\zeta_{-16}}{n_6})^{1/2}$$
$$\times T_2^{-1.02} e^{0.092/T_2} x_{\rm HI}^{-1/2} \quad .$$

Here we have used Eqs. (7), (9), and (11), with $\eta = 1$. It follows that the atomic and molecular mass fractions are equal, ($x_{\rm HI} = 2x_{\rm H_2}$, or $\beta = 2$) for the critical ratio[11]

$$\left(\frac{\zeta_{-16}}{n_6}\right)_{\rm crit} = 10.88\times T_2^{2.03} e^{-0.18/T_2} = 9.02 \quad , \quad (25)$$

Equation (22) is the algebraic equation

$$3.96\left(\frac{\zeta_{-16}}{n_6}\right)^{1/2} x_{\rm HI}^{3/2} T_2^{1.02} e^{-0.092/T_2} = \quad (26)$$
$$[0.96(1+f_3)\frac{1}{1+k_6 x_{\rm HI}/k_{10}x_{\rm H_2}}+0.74]\frac{\zeta_{-16}}{n_6}x_{\rm H_2}$$

The left-hand side is the formation rate per unit volume, and is proportional to $(\zeta/n)^{1/2}$. The right-hand side is the destruction rate per unit volume, and is proportional to ζ/n. For ζ/n less than the critical value given by Eq.(25) the gas becomes molecular in the CRZ, and an HI-to-H_2 transition then occurs in moving from the PDR to the CRZ. For larger ζ/n the gas remains atomic and an HI-to-H_2 transition does not occur.

In Figure 4 we plot the atomic and molecular fractions as functions of ζ_{-16}/n_6 as given by the solution to Eq. (26) (dashed curves) compared to the numerical solutions (solid curves) of the full rate equations within the CRZ. The agreement is excellent. The vertical dotted line indicates the critical ratio of 9.02 as given by Eq. (25). This is close to our numerically computed value of 11.84 indicated by the vertical solid line.

3.4. *Analytic Profiles*

Our procedure to generate analytic profiles is based on the formation-destruction equation

$$x_{\rm HI} = [\frac{1}{2}\alpha f_{\rm shield}(N_{\rm H_2})+\beta]x_{\rm H_2} \quad , \quad (27)$$

and mass conservation

$$x_{\rm HI} + 2x_{\rm H_2} = 1 \quad . \quad (28)$$

With our expressions for α and β (Eqs. [15] and [24]) the local abundances $x_{\rm HI}$ and $x_{\rm H_2}$ may be computed as functions of the molecular column density $N_{\rm H_2}$, for any given ζ/n and $I_{\rm LW}/n$. The parameters α and β themselves depend on $x_{\rm HI}$ and $x_{\rm H_2}$. We integrate Eq.(27) assuming

[11] This expression for the critical ionization to density ratio is more accurate than Eq. 21 in Bialy & Sternberg (2015) for which $x_{\rm HI} = 2x_{\rm H_2}$ at $\zeta_{-16}/n_6 = 11.4$. In that paper we made the approximations $f_d = 1$, and $1 + f_3 = 2$, and we set the cosmic-ray dissociation rate to 0.1ζ (as incorrectly listed in UMIST12) rather than to 0.7ζ as here.

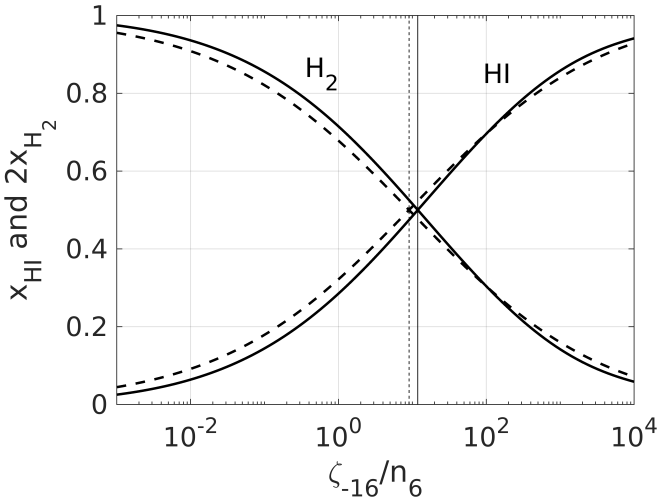


FIG. 4.— Atomic and molecular gas mass fractions, $x_{\rm HI}$ and $2x_{\rm H_2}$, as functions of ζ_{-16}/n_6 (for $T_2 = 1$) as given by solutions to Eq. (26) (dashed curves), and the numerical solutions to the full set of rate equations (solid curves). The vertical dashed and solid lines indicate the critical value as given by the analytic Eq. (25) and the numerical solutions respectively.

that they are constant, writing them as $\bar{\alpha}$ and $\bar{\beta}$ independent of cloud depth, and assuming no CR attenuation. For $\bar{\alpha}$, we set $x_{\rm HI} = 1$ in Eq.(15). For $\bar{\beta}$, and for any ζ_{-16}/n_6, we set f_d as given by Eq.(7) for the constant (asymptotic) $x_{\rm HI}/x_{\rm H_2}$ ratio in the optically thick CRZ. We have computed f_d and $\bar{\beta}$, using our full numerical solutions for $x_{\rm HI}/x_{\rm H_2}$ in the CRZ shown in Figure 4. We find that for 50 K $< T <$ 10^3 K the power-law fit

$$\bar{\beta} = 0.75\times(\frac{\zeta_{-16}}{n_6})^{0.37} T_2^{-0.79} \quad (29)$$

is accurate to within 11% for $0.1 < \zeta_{-16}/n_6 < 10$ and 34% for $0.01 < \zeta_{-16}/n_6 < 100$. With these approximations,

$$N_{\rm HI}(N_{\rm H_2}) = \frac{\bar{\alpha}}{2}\frac{W_d(N_{\rm H_2})}{\sigma_d} + \bar{\beta}N_{\rm H_2} \quad . \quad (30)$$

The first term on the right is the atomic column built up in the PDR, the second term is the column built up in the CRZ.

The depth-dependent atomic and molecular densities may then be constructed in the following simple procedure:

1. Select the ratios $I_{\rm LW}/n$, and ζ/n.
2. Compute $\bar{\alpha}$ using Eq. (15) assuming $x_{\rm HI} = 1$.
3. Compute $\bar{\beta}$ using Eq. (29) given the assumed ζ/n.
4. Solve Eqs. (27) and (28) for $x_{\rm HI}$ and $x_{\rm H_2}$, using $\bar{\alpha}$ and $\bar{\beta}$, given any $N_{\rm H_2}$ and the shielding function Eq. (3).
5. Compute $N_{\rm HI}(N_{\rm H_2})$ using Eq. (18) and with Eq. (4) for $W_d(N_{\rm H_2})$.
6. Plot the density profiles $x_{\rm HI}(N)$ and $x_{\rm H_2}(N)$, with $N = N_{\rm HI} + 2N_{\rm H_2}$.

As we demonstrate below, this procedure provides an accurate representation for the density profiles and HI-to-H_2 transition points for models without CR attenuation, compared to full numerical solutions to the depth-dependent rate equations for the hydrogen/helium network.

3.5. *Timescales*

We have been assuming steady-state conditions for the atomic and molecular densities. The time-scales required to reach a steady-state equilibrium may be estimated by considering the time-dependent H_2 formation-destruction equation (Goldsmith et al. 2007; Liszt 2007). In our problem this may be written as

$$\frac{dx_{\rm H_2}}{d\tau} = 1 - [2 + \frac{1}{2}\alpha f_{\rm shield}(N_{\rm H_2}) + \beta]x_{\rm H_2} \qquad (31)$$

where here the dimensionless time $d\tau \equiv R_- n dt$. Making the assumption that α and β are independent of $x_{\rm HI}$ and $x_{\rm H_2}$ as the system evolves, e.g. by setting $\alpha = \bar{\alpha}$ and $\beta = \bar{\beta}$, the solution is

$$x_{\rm H_2} = 1/a + [x_{\rm H_2}(0) - 1/a)]e^{-a\tau} \qquad (32)$$

where $x_{\rm H_2}(0)$ is the initial molecular fraction, and

$$a \equiv 2 + \frac{1}{2}\bar{\alpha} f_{\rm shield}(N_{\rm H_2}) + \bar{\beta} \quad .$$

The HI-to-H_2 equilibration time scale for any shielding column $N_{\rm H_2}$ is then

$$\tau_{\rm eq} = \frac{1}{a} \quad , \qquad (33)$$

or

$$t_{\rm eq} = \frac{t_{\rm H_2}}{a} = \frac{1}{R_- n} \times \frac{1}{2 + \frac{1}{2}\bar{\alpha} f_{\rm shield} + \bar{\beta}} \quad , \qquad (34)$$

where the H_2 formation time

$$t_{\rm H_2} \equiv \frac{1}{R_- n} = \frac{8.0 \times 10^7}{n_6}\left(\frac{\zeta_{-16}}{n_6}\right)^{-1/2} x_{\rm HI}^{-1/2} T_2^{-1.02} \ \ {\rm yr} \qquad (35)$$

using Eq.(12) for R_-.

In general, $\alpha \gg 1$ and β is of order unity (see Eqs. [15] and [24]). Therefore, in the outer PDR where $f_{\rm shield} \to 1$, $a \gg 1$, and the equilibration time-scale is short, with

$$t_{\rm eq} \approx \frac{2}{D_0} = \frac{1.1 \times 10^3}{I_{\rm LW}} \ \ {\rm yr} \quad . \qquad (36)$$

In this limit the equilibration time is the dissociation time, independent of the gas density. If the gas is initially molecular ($x_{\rm H_2}(0) = 1/2$) photodissociation to the equilibrium atomic state is rapid. Or, if initially fully atomic ($x_{\rm H_2}(0) = 0$) the small equilibrium molecular abundance is reached within a short time. In the inner shielded CRZ, where $f_{\rm shield} \to 0$, and with $\beta \lesssim 1$, we have $a \approx 1/2$, and

$$t_{\rm eq} \approx \frac{1}{2R_- n} = \frac{3.96 \times 10^7}{n_6}\left(\frac{\zeta_{-16}}{n_6}\right)^{-1/2} x_{\rm HI}^{-1/2} T_2^{-1.02} \ \ {\rm yr} \quad . \qquad (37)$$

The equilibration time is then long and comparable to the H_2 formation time. In this limit, $t_{\rm eq}$ is independent of the photodissociation rate, is inversely proportional to the gas density for fixed ζ/n, and decreases as $\zeta^{-1/2}$ for fixed density.

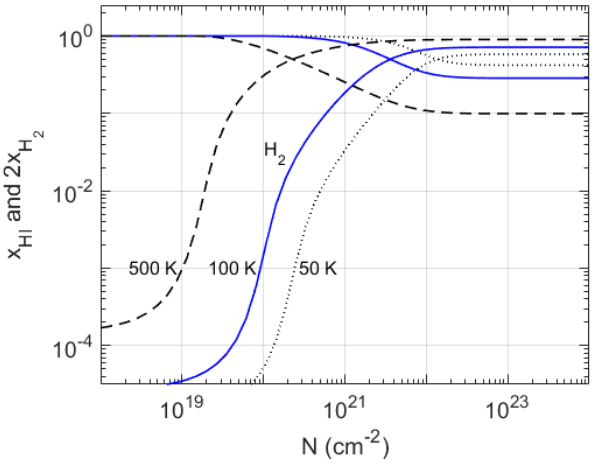


FIG. 5.— The HI and H_2 mass fractions, $x_{\rm HI}$ and $2x_{\rm H_2}$, for our fiducial parameters $I_{\rm LW}/n_6 = 1$ and $\zeta_{-16}/n_6 = 1$, for gas temperatures T=50 K (dotted), 100 K (solid blue), and 500 K (dashed), and no CR attenuation.

For our fiducial parameters, $I_{\rm LW} = \zeta_{-16} = n_6 = T_2 = 1$, we have that $\bar{\alpha} = 1.45 \times 10^5$, and $\bar{\beta} \approx 0.75$. Thus, in the unshielded PDR, $t_{\rm eq} \approx 1.1 \times 10^3$ yr. In the CRZ, $t_{\rm eq} \approx 4.3 \times 10^7$ yr. In Fig. 10, we show computations of the depth-dependent time-scales, short to long, and shown as $n_6 \times t_{eq}$, for a range of $I_{\rm LW}/n_6$ and ζ_{-16}/n_6. We discuss these results as part of our parameter study in §4.4.

4. NUMERICAL MODELS

We now present solutions for the atomic and molecular abundance profiles, and the HI-to-H_2 transition points, obtained by solving the rate equations (Eq. [38]) for our hydrogen-helium chemical network (Figure 1 and Table 1). We refer to these solutions as our "numerical models". We write down the rate equations, and then present our fiducial case and model grid. We compare the results to the "analytic" description we discussed in §3.

4.1. *Rate Equations*

We solve the rate equations for the steady-state abundances, $x_i \equiv n_i/n$ of the atomic and molecular hydrogen/helium species in our chemical network described in §2. Here, n_i is the density of species i, and n is the total hydrogen gas density. The rate equations are

$$\sum_{jl} k_{ijl}(T)\, x_j\, x_l \ + \ \frac{\zeta}{n}\sum_j a_{ij}\, x_j \ + \ \frac{I_{\rm LW}}{n}\sum_j b_{ij}\, x_j$$
$$= x_i \left(\sum_{jl} k_{jil}(T)\, x_l + \frac{\zeta}{n}\sum_j a_{ji} \ + \ \frac{I_{\rm LW}}{n}\sum_j b_{ji} \right) . \qquad (38)$$

The k_{ijl} are the temperature dependent rate coefficients (cm^3 s^{-1}) for two-body reactions of species j and l that lead to the formation of i. We use the rate-coefficients as given in the UMIST2012 database (McElroy et al. 2013), and as updated by Neufeld et al. (2020). We list these in Table 1. The a_{ij} are the direct cosmic-ray ionization

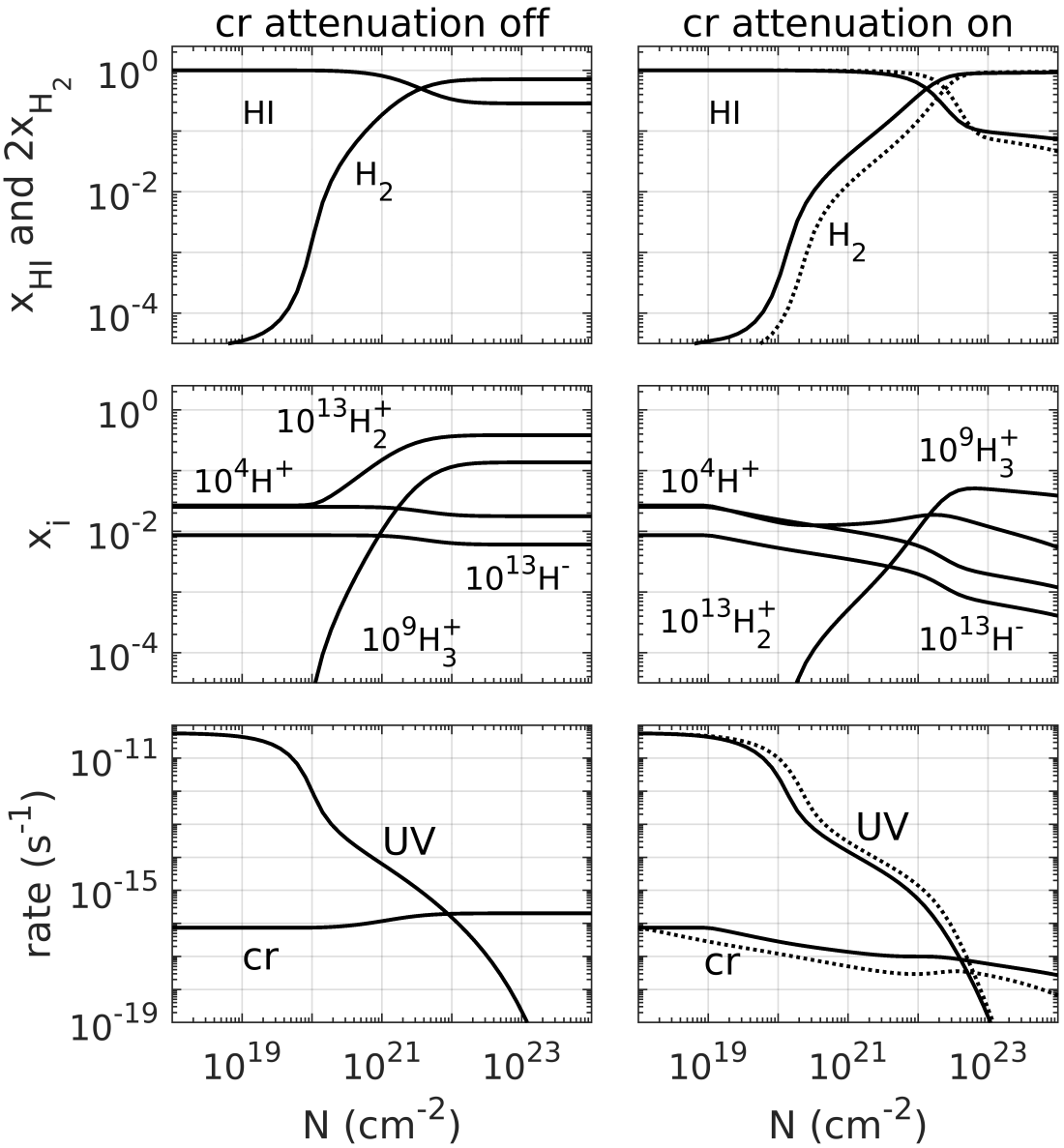


FIG. 6.— Fiducial models for $T_2 = 1$, without (left panels) and with (right panels) CR attenuation. The upper row shows the HI and H_2 mass fractions. For the models with CR attenuation two sets of curves are shown, for magnetic field orientations $\mu = 1$ (solid) and 0.1 (dotted). Middle rows show the fractional abundances of electrons, H^+, H^- and H_3^+ (for $\mu = 1$). The bottom row shows the FUV and CR destruction rates for $\mu = 1$ (solid) and $\mu = 0.1$ (dotted).

and dissociation factors for the five hydrogen/helium CR reactions in our network as listed in Table 2, multiplied by the CR attenuation factor. The b_{ij} are the normalized photorates, for H^- photodetachment, H_2^+ and HeH^+ photodissociation, and local H_2 photodissociation including self-shielding. The incident LW field intensity is specified by $I_{\rm LW}$, and ζ is the cosmic-ray ionization rate at the cloud edge.

Mass conservation is

$$\sum_i \alpha_{im} x_i = X_m \tag{39}$$

where α_{im} is the number of atoms of element m (hydrogen or helium) contained in species i. The hydrogen abundance $X_{\rm H} = 1$ by definition. For helium we assume a cosmic value $X_{\rm He} = 0.1$. Charge conservation is the (dependent) equation

$$\sum q_i x_i = 0 \tag{40}$$

where q_i is the net charge of species i.

For any temperature T, and for a given H_2 column density $N_{\rm H_2}$, the solutions to the rate equations depend on the two ratios $I_{\rm LW}/n$ and ζ/n. $N_{\rm H_2}$ determines the local photodissociation rate via the self-shielding factor. If CR attenuation is included the local solutions also depend on the total gas column $N = N_{\rm HI} + 2N_{\rm H_2}$, but $N_{\rm H_2}$ may still be used as the single independent depth variable. Thus for isothermal conditions the depth-dependent abundance profiles are determined by the two ratios $I_{\rm LW}/n$ and ζ/n at the cloud boundaries. Equations (38) are non-linear, and we solve them numerically by integrating the time dependent differential rate equations to equilibrium, or via Newton iteration of the steady-

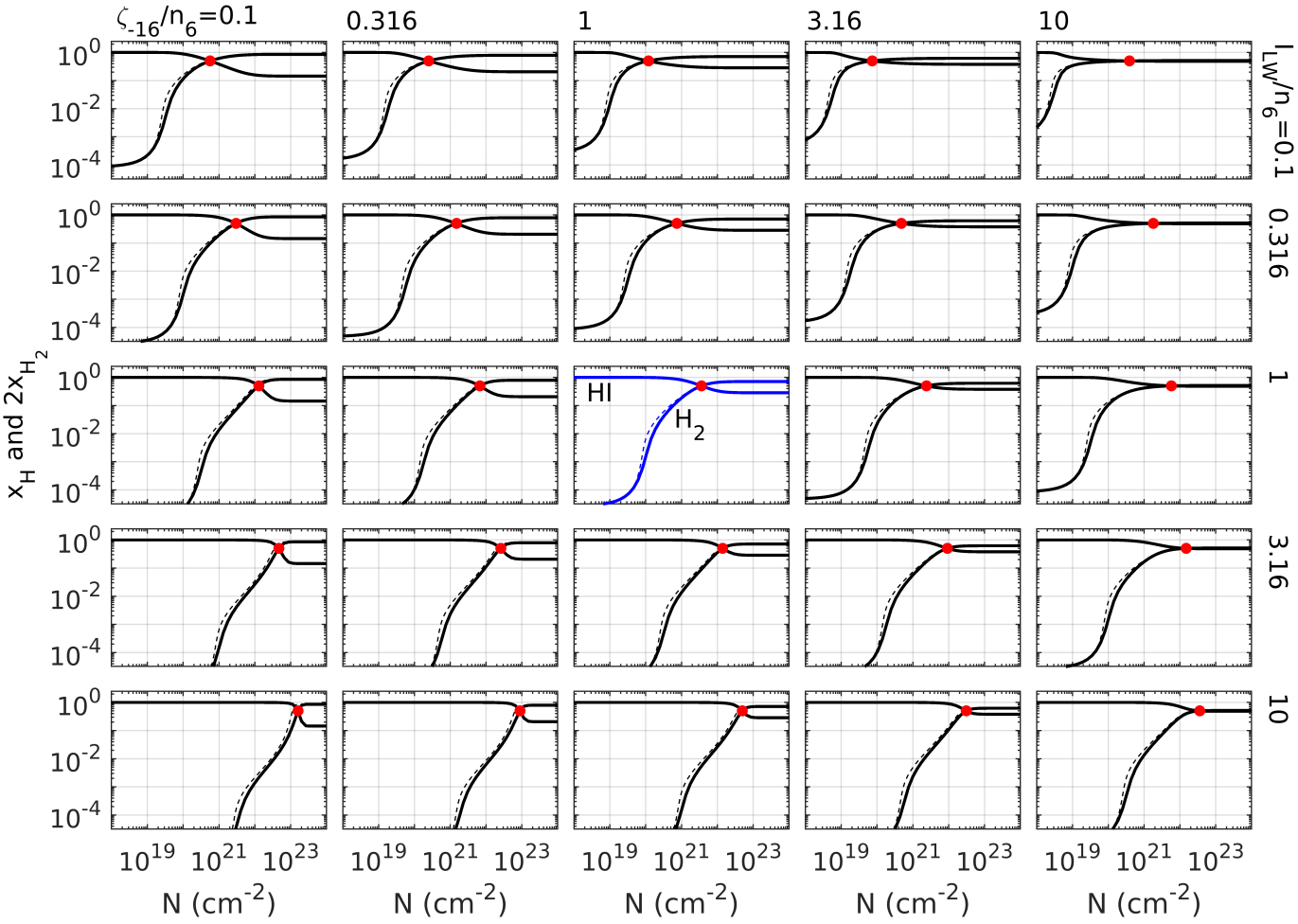


FIG. 7.— Grid of HI and H_2 mass fraction profiles for models without CR attenuation, for $I_{\rm LW}/n_6$ from 0.1 to 10, and ζ_{-16}/n_6 also from 0.1 to 10. The dashed curves are the H_2 mass fractions calculated using the analytic procedure(§3.4). The red markers indicate the HI-to-H_2 transition points where $x_{\rm HI} = 2x_{\rm H_2}$.

state algebraic equations. We compute the species abundances, including $x_{\rm HI}$ and $x_{\rm H_2}$, as functions of cloud depth, integrating inward for $N_{\rm H_2}$ and $N_{\rm HI}$, given the initial conditions $N_{\rm HI} = N_{\rm H_2} = 0$ at the outer boundary. We have verified (as a numerical consistency check) that for fixed temperature the solutions depend only on the ratios $I_{\rm LW}/n$ and ζ/n, for any FUV intensity, cosmic-ray ionization rate, and gas density.

4.2. *Fiducial Case*

For our fiduical parameters we set $I_{\rm LW}/n_6 = 1$ and $\zeta_{-16}/n_6 = 1$. In Figure 5 we show the resulting HI and H_2 mass fractions, $x_{\rm HI}$ and $2x_{\rm H_2}$, as functions of total gas column N (cm^{-2}) for gas temperatures $T = 50$, 100, and 500 K. In these computations we do not include any cosmic-ray attenuation. With these choices, (a) the gas is predominantly atomic in the outer PDR (Eq. [16]), (b) the gas is primarily molecular in the CRZ (Eq. [25]), and (c) the transition points occur at total gas columns $\lesssim 10^{22}$ cm^{-2} (Eq. [20]). The effective gas-phase formation rate coefficient varies linearly with T (Eq. [12]), so as the temperature increases the transition points occur at smaller gas columns, and are at 1.4×10^{22}, 3.7×10^{21}, and 2.3×10^{20} cm^{-2}, for $T = 50$, 100, and 500 K. In the CRZ, the molecular fractions are 0.58, 0.71, and 0.90. It is evident that higher temperatures induce stronger HI-to-H_2 transitions.

In Figure 6 we present more details for the $T = 100$ K case (lefthand panels), and we compare to models that include cosmic-ray attenuation (righthand panels). We set $\zeta_{-16}/n_6 = 1$ at the cloud surface, and assume the $q = 0.385$ power-law (Eq.[5]) for $\zeta(N)$ for the Padovani et al. (2018b) model-$\mathcal{H}$ particle energy distribution. In the upper righthand panel, the solid curves are the HI and H_2 mass fractions assuming any magnetic field is normal to the cloud surface ($\mu = 1$ in Eq.[5])]. The dashed curves are for a highly inclined magnetic field ($\mu \equiv cos\theta = 0.1$).

At the unshielded cloud edge, the molecular fraction $x_{\rm H_2} = 1.3 \times 10^{-5}$ (Eq.[16]) for all three models. Without CR attenuation (upper left panel), the HI-to-H_2 transition point ($x_{\rm HI} = 1/2$) occurs at $N = 4 \times 10^{21}$ cm^{-2}, where $N_{\rm HI} = 2.9 \times 10^{21}$ and $N_{\rm H_2} = 5.7 \times 10^{20}$ cm^{-2}. The HI column at the transition point is consistent with Eq.(20) for the total HI column produced by photodissociation. An HI-to-H_2 transition is expected because $\zeta_{-16}/n_6 < 11.87$ (see Fig. 4). In the CRZ, the atomic and molecular mass fractions are constant, with $x_{\rm HI} = 0.28$, and $2x_{\rm H_2} = 0.72$.

With CR attenuation the transition point is shifted to slightly larger gas columns of 1.31×10^{22} and 2.41×10^{22} cm^{-2}, $\mu = 1$ and 0.1. This is because of the lowered

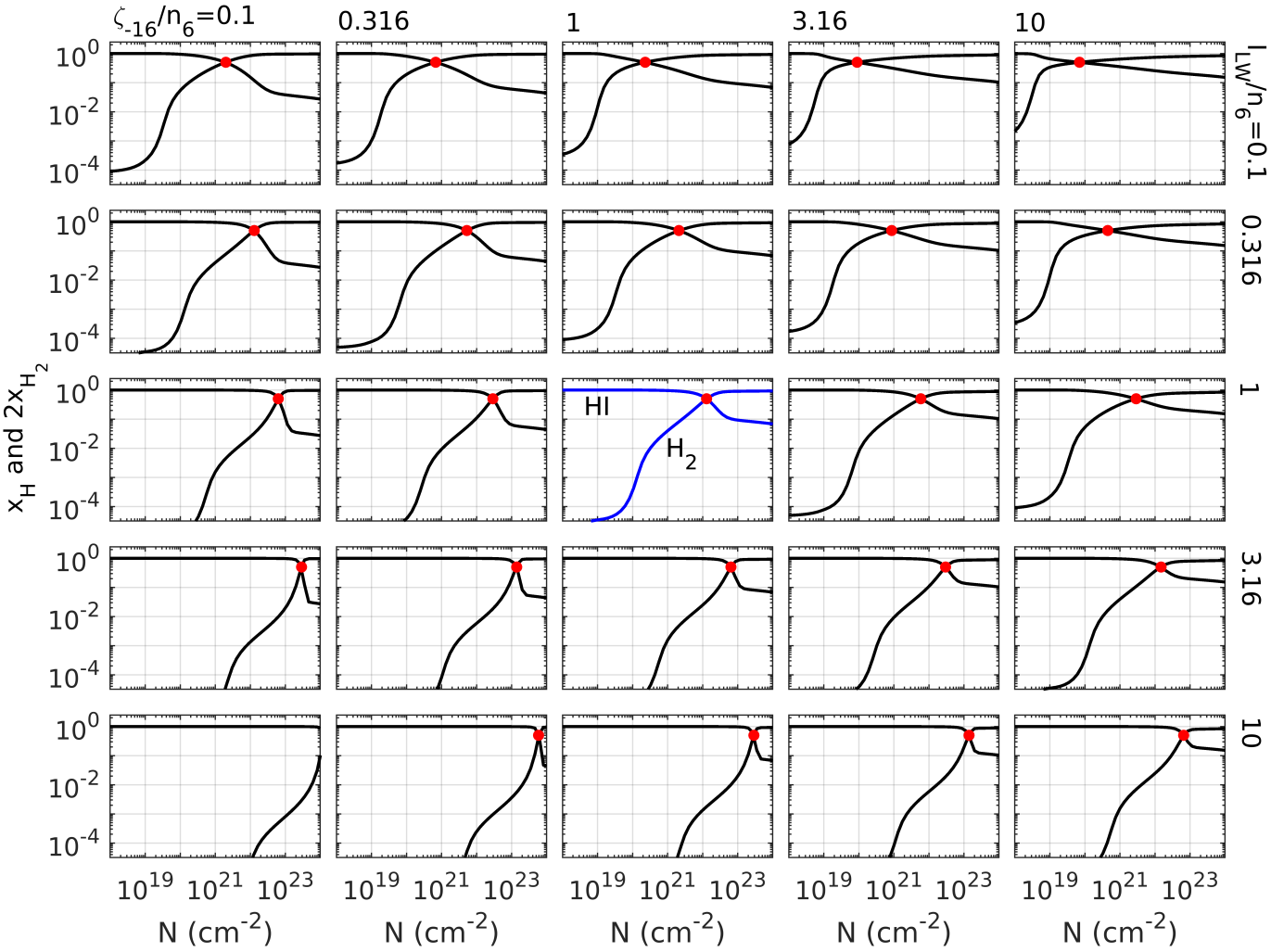


FIG. 8.— Grid of HI and H_2 mass fraction profiles for models including CR attenuation, for $I_{\rm LW}/n_6$ from 0.1 to 10, and ζ_{-16}/n_6 also from 0.1 to 10. The dashed curves are the H_2 mass fractions calculated using the analytic procedure(§3.4). The red markers indicate the HI-to-H_2 transition points where $x_{\rm HI} = 2x_{\rm H_2}$.

ionization rate, and reduction of the effective gas-phase formation rate coefficient R_- (Eq.[12]) within the PDR. In the CRZ, the atomic fractions continue to decrease with depth, in accordance with Eq. (26) and Fig. 4, as ζ decreases and the molecular destruction rate is reduced.

The middle panels of Fig. 6 show the abundances of electrons, H^+, H^-, and H_3^+ ions, without (left) and with (right) CR attenuation. As expected, the protons carry the positive charge and the curves for $x_{\rm e}$ and $x_{\rm H^+}$ overlap. In the PDR, $x_{\rm e} = 2.5 \times 10^{-6}$ as given by Eq.(11). The electron fraction drops in the CRZ, due to the reduced atomic fraction there. The abundance of the H^- intermediary is everywhere proportional to the electron fraction (Eq.[13]). Mutual neutralization [R3] and photodetachment [R4] are negligible compared to associative detachment [R2], and $\eta = 1$. The H_3^+ abundance rises as the H_2 density grows. When CR attenuation is included the H_3^+ abundance declines sightly with depth as the ionization rate is diminished.

The bottom panels of Fig. 6 show the LW photodissociation and CR destruction rates as functions of the total gas column. For both models, the onset of molecular self shielding occurs at $N \approx 5 \times 10^{19}$ cm^{-2} where $N_{\rm H_2} = 2.1{\times}10^{15}$, without CR attenuation, and $1.5{\times}10^{15}$, and 7.2×10^{14} with CR attenuation (for $\mu = 1$ and 0.1), and the photodissociation rate drops with increasing cloud depth. Without CR attenuation the LW and CR destruction rates are equal at $N = 9.3 \times 10^{21}$ cm^{-2}, near to the HI-to-H_2 transition point. The CR destruction rate is slightly larger in the CRZ due to the increase in the f_d branching ratio (Eq.7). With CR attenuation the destruction rates are equal at $3.8{\times}10^{22}$ and $6.6{\times}10^{22}$ cm^{-2} (for $\mu = 1$ and 0.1), and the CR destruction rates continue to decline within the CRZ.

4.3. *Model Grids*

In Figure 7 we present a 5×5 numerical model grid for the HI and H_2 density profiles, for $I_{\rm LW}/n_6$ ranging from 0.1 to 10 in steps of 0.5 dex (rows), and ζ_{-16}/n_6 from 0.1 to 10 (columns) also in steps of 0.5 dex. These computations are all for $T = 100$ K, without CR attenuation. The middle panel (blue curves) is our fiducial model. In Figure 7 we also plot (dashed curves) the H_2 abundances computed using our analytic procedure (§3.4). The agreement between the analytic and numerical results is excellent.

As expected, for fixed ζ_{-16}/n_6, the molecular fractions in the PDRs are reduced as $I_{\rm LW}/n_6$ is increased and

TABLE 5
MODELS WITHOUT COSMIC-RAY ATTENUATION

	$\log(\zeta_{-16}/n_6)$	-1	-0.5	0	0.5	1
	$\log(I_{UV}/n_6)$					
$N_{\rm HI}$ (cm^{-2})	-1	4.1(20)	1.8(20)	8.2(19)	4.8(19)	2.1(20)
$N_{\rm H_2}$ (cm^{-2})		7.7(19)	3.5(19)	1.8(19)	1.3(19)	9.2(19)
$N_{\rm tran}$ (cm^{-2})		5.6(20)	2.5(20)	1.2(20)	7.4(19)	3.9(20)
$f_{\rm shield}$		6.5(-5)	1.1(-4)	1.6(-4)	1.9(-4)	5.7(-5)
$n_6 \times t_{\rm eq}$ (yr)		7.7(7)	4.3(7)	2.5(7)	1.4(7)	8.0(6)
	-0.5	2.3(21)	1.1(21)	5.2(20)	3.1(20)	9.5(20)
		3.6(20)	2.0(20)	1.1(20)	8.5(19)	4.1(20)
		3.0(21)	1.5(21)	7.4(20)	4.8(20)	1.8(21)
		2.0(-5)	3.3(-5)	5.1(-5)	6.1(-5)	1.8(-5)
		7.7(7)	4.4(7)	2.5(7)	1.4(7)	8.0(6)
	0	1.0(22)	5.2(21)	2.7(21)	1.6(21)	3.2(21)
		1.2(21)	7.4(20)	4.8(20)	3.8(20)	1.3(21)
		1.3(22)	6.7(21)	3.6(21)	2.4(21)	5.8(21)
		6.4(-6)	1.0(-5)	1.6(-5)	1.9(-5)	5.7(-6)
		7.7(7)	4.4(7)	2.5(7)	1.4(7)	8.0(6)
	0.5	4.1(22)	2.1(22)	1.1(22)	6.7(21)	9.0(21)
		2.9(21)	2.1(21)	1.5(21)	1.2(21)	3.0(21)
		4.7(22)	2.6(22)	1.4(22)	9.2(21)	1.5(22)
		1.9(-6)	3.1(-6)	4.8(-6)	6.1(-6)	1.8(-6)
		7.7(7)	4.4(7)	2.5(7)	1.4(7)	8.0(6)
	1	1.5(23)	8.0(22)	4.3(22)	2.5(22)	2.4(22)
		6.6(21)	4.4(21)	3.2(21)	3.1(21)	6.0(21)
		1.6(23)	8.9(22)	5.0(22)	3.1(22)	3.6(22)
		4.4(-7)	9.7(-7)	1.6(-6)	1.7(-6)	5.4(-7)
		8.9(7)	4.4(7)	2.5(7)	1.4(7)	8.0(6)

The HI, H_2, and total hydrogen column densities, $N_{\rm tran}$, at the transition points, for each model in the grid shown in Figure 7. These are models without CR attenuation. The shielding factors and the timescales at the transition points are also listed for each model. Numbers in parentheses are exponents. For example, $4.1(20) = 4.1 \times 10^{20}$.

photodissociation becomes more effective relative to the fixed formation rates (Eq. [16]). The transition points (indicated by the red markers) therefore occur at larger gas columns as $I_{\rm LW}/n_6$ is increased. For example, for $\zeta_{-16}/n_6 = 1$, and for $I_{\rm LW}/n_6$ from 0.1 to 10, the molecular fraction ranges from 1.26×10^{-4} to 1.26×10^{-6} at the cloud edges. The transition columns increase from 1.2×10^{20} to 5×10^{22} cm^{-2}. The molecular fractions remain unaltered in the CRZs (Eq.[26] and Figure 4), where $2x_{\rm H_2} = 0.71$ and $x_{\rm HI} = 0.29$, independent of $I_{\rm UV}/n_6$.

For increasing ζ_{-16}/n_6 at fixed $I_{\rm LW}/n_6$, the molecular fractions increase in the PDRs but decrease in the CRZs. This is because the H_2 formation efficiency via CR ionization is enhanced for larger ζ/n, relative to the fixed photodissociation rates in the PDR (Eq. [16]). However, in the CRZ the molecular fraction decreases with ζ/n because removal by CR ionization is more effective than CR driven formation (Eq. [26]] and Figure 4). The transition columns therefore first *decrease* for increasing ζ_{-16}/n_6, but above $(\zeta_{-16}/n_6)_{\rm crit}$=11.84 (see Fig. 4) a conversion point does not occur and the gas remains predominantly atomic in the CRZ. For example, for $I_{\rm LW}/n_6 = 1$, and for ζ_{-16}/n_6 from 0.1 to 10, the H_2 mass fraction at the PDR edge increases from 8.38×10^{-6} to 8.38×10^{-5}. In the CRZ, it decreases from 0.86 to 0.52. For ζ_{-16}/n_6 from 0.1 to 3.16, the transition column decreases from 1.27×10^{22} to $\sim 2.38 \times 10^{21}$. For $\zeta_{-16}/n_6 = 10$ a transition just barely occurs at 5.81×10^{21} cm^{-2}.

In Table 5 we list the HI and H_2 column densities, and the total hydrogen column, at the atomic to molecular transition points ($x_{\rm HI} = 2x_{\rm H_2}$) for each of the models in the grid. The required H_2 shielding columns range from $\sim 10^{19}$ to a few 10^{21} cm^{-2}, corresponding to shielding factors, $f_{\rm shield}$, from 1.9×10^{-4} to 4.4×10^{-7}. We also list the equilibration timescales required to reach the transition points, assuming fully atomic initial states. These range from $n_6 \times t_{\rm eq} = 8.0 \times 10^6$ to 8.9×10^7 yr.

In Figure 9 (left panel) we plot the hydrogen gas columns at which the transition points occur, as functions of ζ_{-16}/n_6 for the various $I_{\rm UV}/n_6$ ratios, for models without CR attenuation. For $I_{\rm UV}/n_6 = 1$, the transition column decreases from 3.62×10^{22} to a minimum of 2.2×10^{21}cm^{-2}, for ζ_{-16}/n_6 from 0.01 to 3.8, and then rises again and diverges at $(\zeta_{-16}/n_6)_{\rm crit} = 11.84$ beyond which complete transitions no longer occur. The rise as ζ_{-16}/n_6 approaches the critical value (indicated by the vertical dashed line) is due to the additional contribution of cosmic ray H_2 destruction near the inner edge of the PDR, which moderates the shape of the transition profile.

In Figure 8, we display the 5×5 model grid, now in-

TABLE 6
MODELS WITH COSMIC-RAY ATTENUATION

	$\log(\zeta_{-16}/n_6)$	-1	-0.5	0	0.5	1
	$\log(I_{UV}/n_6)$					
$N_{\rm HI}$ ($\rm cm^{-2}$)	-1	1.4(21)	4.6(20)	1.5(20)	5.7(19)	4.2(19)
$N_{\rm H_2}$ ($\rm cm^{-2}$)		2.9(20)	1.1(20)	3.9(19)	1.6(19)	1.4(19)
$N_{\rm tran}$ ($\rm cm^{-2}$)		2.0(21)	6.8(20)	2.3(20)	8.9(19)	7.0(19)
$f_{\rm shield}$		2.4(-5)	5.1(-5)	1.0(-4)	1.7(-4)	1.8(-4)
$n_6 \times t_{\rm eq}$ (yr)		2.2(8)	1.0(8)	4.6(7)	2.2(7)	1.2(7)
	-0.5	1.0(22)	3.9(21)	1.5(21)	5.7(20)	2.8(20)
		1.4(21)	6.9(20)	3.2(20)	1.5(20)	8.6(19)
		1.3(22)	5.3(21)	2.1(21)	8.7(20)	4.5(20)
		5.3(-6)	1.1(-5)	2.2(-5)	4.1(-5)	6.0(-5)
		3.2(8)	1.5(8)	7.0(7)	3.3(7)	1.7(7)
	0	5.5(22)	2.4(22)	1.0(22)	4.3(21)	1.9(21)
		3.9(21)	2.4(21)	1.4(21)	8.0(20)	4.6(20)
		6.3(22)	2.9(22)	1.3(22)	5.9(21)	2.9(21)
		1.2(-6)	2.5(-6)	4.9(-6)	9.6(-6)	1.6(-5)
		4.5(8)	2.1(8)	1.0(8)	4.9(7)	2.4(7)
	0.5	2.7(23)	1.2(23)	5.6(22)	2.5(22)	1.1(22)
		9.9(21)	6.2(21)	3.9(21)	2.6(21)	1.7(21)
		2.9(23)	1.4(23)	6.4(22)	3.0(22)	1.5(22)
		1.8(-7)	5.1(-7)	1.2(-6)	2.2(-6)	4.0(-6)
		8.4(8)	3.2(8)	1.4(8)	6.9(7)	3.3(7)
	1	1.2(24)	5.7(23)	2.7(23)	1.2(23)	5.8(22)
		1.9(22)	1.1(22)	1.0(22)	6.4(21)	4.2(21)
		1.2(24)	5.9(23)	2.9(23)	1.4(23)	6.6(22)
		3.2(-8)	1.4(-7)	1.7(-7)	4.8(-7)	1.0(-6)
		1.5(9)	3.8(8)	2.5(8)	9.9(7)	4.4(7)

The HI, H_2, and total hydrogen column densities, $N_{\rm tran}$, at the transition points, for each model in the grid shown in Figure 8. These are models with CR attenuation. The shielding factors and the timescales at the transition points are also listed for each model.

cluding CR attenuation. For these models, we again use Equation (5) assuming Padovani model-$\mathcal{H}$ ($q = 0.385$) for a normally inclined magnetic field ($\mu = 1$). The atomic fractions in the PDRs are increased, and the transition points generally occur at greater depths, due to the lowered ionization and reduced H_2 formation rates through the PDRs. However, in the CRZs, the molecular fractions are always larger for models with CR attenuation because of the reduced H_2 destruction rates, and transitions always occur.

In Table 6 we list the HI, H_2, and total hydrogen column densities at the transition points for the model grid shown in Figure 8, as well as the shielding factors and equilibration timescales. As expected, with CR attenuation the required H_2 shielding columns are larger, reaching up to $\sim 10^{22}$ $\rm cm^{-2}$, corresponding to $f_{\rm shield} = 1.7 \times 10^{-7}$.

Figure 9 (right panel) shows the hydrogen gas columns (solid curves) at the transition points for models with CR attenuation, as functions of the ionization rate to density ratio at the cloud edge, $(\zeta_{-16}/n_6)_{\rm edge}$, for the various $I_{\rm UV}/n_6$ for models including CR attenuation. For any $I_{\rm UV}/n_6$ the transition columns initially decrease with $(\zeta_{-16}/n_6)_{\rm edge}$ due to the overall enhanced ionization and molecular formation rates in the PDRs. For these branches the atomic to molecular transitions are governed by self-shielding of the H_2 against LW photodissociation. The (dotted) lines in Figure 9 are contours of constant local attenuated ratios ζ_{-16}/n_6, for our assumed CR attenuation function. The intersections with the solid curves give the local attenuated values of ζ_{-16}/n_6 at the transition points. For example, for $I_{\rm UV}/n_6 = 1$, and $(\zeta_{-16}/n_6)_{\rm edge} = 1.52$, the transition point is at 8.4×10^{21} $\rm cm^{-2}$ where locally $\zeta_{-16}/n_6 = 0.1$. The solid curves start rising with $(\zeta_{-16/n_6})_{\rm edge}$ when the transitions occur within the CRZs. The local values of ζ_{-16}/n_6 must then equal $(\zeta_{-16}/n_6)_{\rm crit} = 11.84$ (see Figure 4), so the curves all converge to a line running along this local ζ_{-16}/n_6 contour (close to 10).

4.4. *Depth-dependent time scales*

Figure 10 shows the depth-dependent equilibration time-scales, plotted as the product $n_6 t_{\rm eq}$ (Eq. [34]) versus gas column density N. These are for models without CR attenuation. We compute α and β locally at every depth (rather than using $\bar{\alpha}$ and $\bar{\beta}$). As expected, for fixed $I_{\rm LW}/n_6 = 1$ (top panel) the time scale approaches the short dissociation limit of $n_6 t_{\rm eq} \approx 1.1 \times 10^3 / I_{\rm LW}$ yr in the PDR at low gas columns, independent of ζ_{-16}/n_6. At large depths in the CRZ, the time scale approaches the long H_2 formation limit, with $n_6 t_{\rm eq} \approx 4 \times 10^7 (\zeta_{-16}/n_6)^{-1/2}$ yr. At intermediate gas columns, e.g. at 10^{20} $\rm cm^{-2}$ in Fig. 10, the time-scale *increases* with ζ/n because elevating the H_2 formation rate

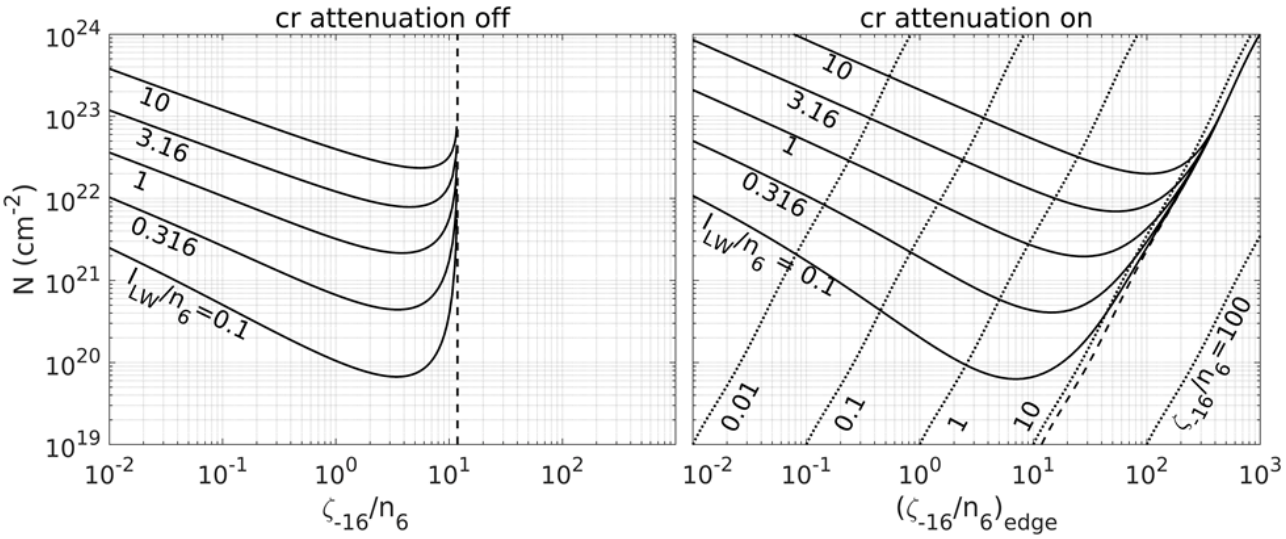


FIG. 9.— Left panel: Total hydrogen gas columns at the atomic to molecular transition points as functions of ζ_{-16}/n_6, for $I_{\rm LW}/n_6$ ranging from 0.1 to 10, for models without CR attenuation. The vertical dashed line indicates the critical ratio $\zeta_{-16}/n_{6\rm crit} = 11.84$ (at 100 K). Right panel: Transition columns for models with CR attenuation (for $\mu = 1$). The dotted lines are contours of constant local attenuated ζ_{-16}/n_6. The dashed line is the contour for the critical value.

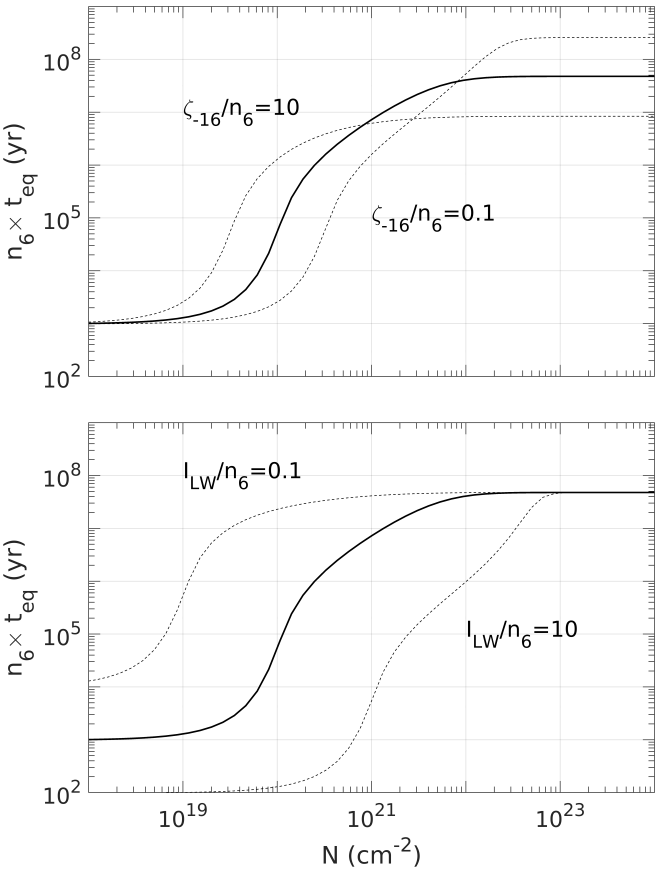


FIG. 10.— Depth-dependent equilibration time-scales for $I_{\rm LW}/n_6 = 1$ with ζ_{-16}/n_6 from 0.1 to 10 (upper panel), and for $\zeta_{-16}/n_6 = 1$, with $I_{\rm LW}/n_6$ from 0.1 to 10 (lower panel).

within the PDR increases the shielding column, thereby reducing the dissociation rate and associated equilibration time. At fixed $\zeta_{-16}/n_6 = 1$ (bottom panel) the product $n_6 t_{\rm eq}$ decreases linearly with $I_{\rm LW}/n_6$ at the cloud edges in the dissociation limit. The time-scale lengthens as self-shielding sets in, finally reaching the long H_2 formation time in the CRZ, independent of $I_{\rm LW}/n_6$.

5. SUMMARY AND DISCUSSION

We have presented an analytic and numerical study of the atomic and molecular hydrogen density profiles, and (HI-to-H_2) transitions that may occur in dense, dust-free (primoridal) interstellar photodissociation regions (PDRs) and optically thick cosmic-ray zones (CRZs). Our models are highly idealized. We focus on 1D, steady-state, cold, isothermal, constant density gas slabs, irradiated by stellar-type far-UV radiation fields, and fluxes of non-thermal cosmic-ray particles. Molecular hydrogen formation is by ionization driven gas phase (two-body) chemistry only, primarily via the H^- intermediary, rather than by dust-catalysis as in standard ISM clouds. H_2 absorption line self-shielding enables the atomic to molecular transitions, even without any dust opacity.

For this idealized set-up we solve the rate equations for the depth-dependent abundances of HI and H_2, as well as the trace species, H^+, H_2^+, H_3^+, H^-, He, He^+, HeH^+ and electrons. The basic parameters in the problem are, (a) the unattenuated LW radiation field intensity I_{LW}, (b) the gas density n, (c) the cosmic-ray ionization rate ζ, and (d) the gas temperature T. For any temperature, the depth dependent abundances and the HI-to-H_2 transition points depend on the two ratios I_{LW}/n and ζ/n. The cosmic-ray driven gas phase H_2 formation route may be represented by an effective rate coefficient R_- depending on the ionization fraction (Equations [6]-[9]).

Because gas phase H_2 formation is inefficient compared to molecule production on dust-grain surfaces, we focus on relatively dense gas for which the formation rates are enhanced. Our fiducial model is for $n = 10^6$ cm^{-3} at $T = 100$ K. The illuminating FUV radiation is for a (Pop III) 10^5 K blackbody field normalized to a Galactic interstellar LW intensity, $I_{\rm LW} = 1$, with LW flux 2.07×10^7 photons cm $^{-2}$ s^{-1}. The H_2 cosmic-ray ionization rate $\zeta = 10^{-16}$ s^{-1}. We also present results for I_{LW}/n and ζ/n ranging ± 1 dex around our fiducial case. For this range of parameters, H^- photodetach-

ment is negligible, and the resulting HI and H_2 density profiles are insensitive to the IR to UV spectral shapes of the radiation fields. For our fiducial model an HI-to-H_2 transition occurs at a total hydrogen gas column density of 4×10^{21} cm^{-2}, within an equilibration time-scale of 3×10^7 yr. This is comparable to the transition column and H_2 formation time for typical dusty Galactic clouds with densities $\sim 10^2$ cm^{-3}.

We examine the effects of cosmic-ray energy losses on the HI and H_2 density profiles and transition points. CR attenuation moves the transition points to larger cloud depths due to the reduced ionization fractions and lowered molecular formation efficiencies in the PDRs. However, in the CRZs, the reduced cosmic-ray destruction rates lead to enhanced molecular fractions.

For our parameter space, the dust-free limit is reached for dust-to-gas ratios $Z'_d \lesssim 10^{-5}$ (relative to Galactic), depending slightly on the ionization rate and gas density. In this limit, gas-phase H_2 formation dominates, and dust-gas neutralization processes do not affect the hydrogen-helium chemistry and ionization structures. Given the probable super-linear dependence of interstellar dust-to-gas mass ratios on the ambient metallicities in differing environments, the dust-free limit may be reached for metallicities $Z' \lesssim 10^{-2}$ (relative to Solar) depending slightly on gas density and ionization rate.

Our theoretical study is relevant for systems such as low metallicity dwarf galaxies at low- and high redshift, possibly dense condensations in the circumgalactic medium of galaxies, and intergalactic filaments, as well as for protoplanetary disks and dust-depleted outflow jets from protostars. As for dusty systems, the long H_2 formation time scales suggest that cloud evolution, dynamical turbulence, and variability of the radiation sources must be considered for a complete description of the HI and H_2 abundances in specific astrophysical systems.

Acknowledgements: We thank Frank Le Petit, David Neufeld, and Marco Padovani for helpful discussions and advice. We thank the referee for constructive and helpful comments. This work was supported by the German-Science Foundation via DFG/DIP grant STE/1869-2 GE 625/17-1, by the Center for Computational Astrophysics (CCA) of the Flatiron Institute, and the Mathematics and Physical Sciences (MPS) division of the Simons Foundation, USA.

REFERENCES

Abel, T., Bryan, G. L., & Norman, M. L. 2002, Modes Star Form. Orig. F. Popul. Astron. Soc. Pacific Conf. Ser., 285
Barlow, S. E. 1984, PhD Thesis, University of Colorado, Boulder CO
Bialy, S. 2020, ApJ, 62
Bialy, S. & Sternberg, A. 2015, MNRAS, 450, 4424
—. 2016, ApJ, 822, 83
—. 2019, ApJ, 881, 160
Bisbas, T. G., van Dishoeck, E. F., Papadopoulos, P. P., Szűcs, L., Bialy, S., & Zhang, Z.-Y. 2017, ApJ, 839, 90
Black, J. H. & van Dishoeck, E. F. 1987, ApJ, 322, 412
Bohme, D. K., Mackay, G. I., & Schiff, H. I. 1980, J. Chem. Phys., 73, 4976
Bruhns, H., Kreckel, H., Miller, K. A., Urbain, X., & Savin, D. W. 2010, Phys. Rev. A, 82, 042708
Cravens, T. E. & Dalgarno, A. 1978, ApJ, 219, 750
Cummings, A. C., Stone, E. C., Heikkila, B. C., Lal, N., Webber, W. R., Jóhannesson, G., Moskalenko, I. V., Orlando, E., & Porter, T. A. 2016, ApJ, 831, 18
Cuppen, H. M., Ioppolo, S., Romanzin, C., & Linnartz, H. 2010, Phys. Chem. Chem. Phys. PCCP, 12, 12077
Dalgarno, A. 2006, Proc. Natl. Acad. Sci. United States Am., 103, 12269
Dalgarno, A. & McCray, R. A. 1973, ApJ, 181, 95
de Jong, T. 1972, A&A, 20
Draine, B. T. 1978, ApJS, 36, 595
Draine, B. T. & Bertoldi, F. 1996, ApJ, 468, 269
Ercolano, B. & Storey, P. J. 2006, MNRAS, 372, 1875
Esposito, F., Coppola, C. M., & De Fazio, D. 2015, Journal of Physical Chemistry A, 119, 12615
Federman, S. R., Glassgold, A. E., & Kwan, J. 1979, ApJ, 227, 466
Galli, D. & Palla, F. 2013, ARA&A, 51, 163
Girichidis, P., Offner, S. S., Kritsuk, A. G., Klessen, R. S., Hennebelle, P., Kruijssen, J. M., Krause, M. G., Glover, S. C., & Padovani, M. 2020, Sp. Sci. Rev., 216, 68
Glassgold, A. E., Najita, J., & Igea, J. 2004, ApJ, 615, 972
Glover, S. C. O. 2003, ApJ, 584, 331
Goldsmith, P. F. & Li, D. 2005, ApJ, 622, 938
Goldsmith, P. F., Li, D., & Krčo, M. 2007, ApJ, 654, 273
Gould, R. J. & Salpeter, E. E. 1963, ApJ, 138, 393
Güsten, R., Wiesemeyer, H., Neufeld, D., Menten, K. M., Graf, U. U., Jacobs, K., Klein, B., Ricken, O., Risacher, C., & Stutzki, J. 2019, Nature, 568, 357
Haardt, F. & Madau, P. 2012, ApJ, 746, 125
Haiman, Z. 2016, in Underst. Epoch Cosm. Reionization Challenges Prog., Vol. 423, 1–22
Haiman, Z., Rees, M. J., & Loeb, A. 1997, ApJ, 476, 458
Harada, N. & Herbst, E. 2008, ApJ, 685, 272
Herbst, E., Bohme, D. K., Payzant, J. D., & Schiff, H. I. 1975, ApJ, 201, 603
Herbst, E. & Klemperer, W. 1973, ApJ, 185, 505
Ivlev, A. V., Dogiel, V. A., Chernyshov, D. O., Caselli, P., Ko, C. M., & Cheng, K. S. 2018, ApJ, 855, 23
Jura, M. 1974, ApJ, 191, 375
Juřek, M., Špirko, V., & Kraemer, W. P. 1995, Chemical Physics, 193, 287
Karpas, Z., Anicich, V., & Huntress, W. T. 1979, J. Chem. Phys., 70, 2877
Larsson, M., Geppert, W. D., & Nyman, G. 2012, Reports Prog. Phys., 75
Latif, M. A., Bovino, S., Grassi, T., Schleicher, D. R. G., & Spaans, M. 2014, MNRAS, 446, 3163
Le Bourlot, J., Le Petit, F., Pinto, C., Roueff, E., & Roy, F. 2012, A&A, 541, A76
Lepp, S., Dalgarno, A., van Dishoeck, E. F., & Black, J. H. 1988, ApJ, 329, 418
Lepp, S., Stancil, P. C., & Dalgarno, A. 2002, J. Phys. B At. Mol. Opt. Phys., 35, R47
Li, D. & Goldsmith, P. F. 2003, ApJ, 585, 823
Li, Q., Narayanan, D., & Davé, R. 2019, MNRAS, 490, 1425
Liszt, H. S. 2007, A&A, 461, 205
Martin, P. G., Schwarz, D. H., & Mandy, M. E. 1996, ApJ, 461, 265
Mashian, N., Sternberg, A., & Loeb, A. 2013, MNRAS, 435, 2407
Mathis, J. S., Mezger, P. G., & Panagia, N. 1983, A&A, 128, 212
McCall, B. J., Huneycutt, A. J., Saykally, R. J., Djuric, N., Dunn, G. H., Semaniak, J., Novotny, O., Al-Khalili, A., Ehlerding, A., Hellberg, F., Kalhori, S., Neau, A., Thomas, R. D., Paal, A., Österdahl, F., & Larsson, M. 2004, Phys. Rev. A, 70, 052716
McDowell, M. R. C. 1961, Obs., 81, 240
McElroy, D., Walsh, C., Markwick, A. J., Cordiner, M. A., Smith, K., & Millar, T. J. 2013, A&A, 550, A36
McKee, C. F. & Krumholz, M. R. 2010, ApJ, 709, 308
Miyake, S., Stancil, P. C., Sadeghpour, H. R., Dalgarno, A., McLaughlin, B. M., & Forrey, R. C. 2010, ApJ, 709, L168
Neufeld, D. A., Goto, M., Geballe, T. R., Güsten, R., Menten, K. M., & Wiesemeyer, H. 2020, ApJ, 894, 37
Neufeld, D. A. & Wolfire, M. G. 2017, ApJ, 845, 163

Novotný, O., Wilhelm, P., Paul, D., Kálosi, Á., Saurabh, S., Becker, A., Blaum, K., George, S., Göck, J., Grieser, M., Grussie, F., von Hahn, R., Krantz, C., Kreckel, H., Meyer, C., Mishra, P. M., Muell, D., Nuesslein, F., Orlov, D. A., Rimmler, M., Schmidt, V. C., Shornikov, A., Terekhov, A. S., Vogel, S., Zajfman, D., & Wolf, A. 2019, Science, 365, 676
Öberg, K. I. & Bergin, E. A. 2021, Phys. Rep., 893, 1
Padovani, M., Galli, D., & Glassgold, A. E. 2009, A&A, 501, 619
Padovani, M., Galli, D., Ivlev, A. V., Caselli, P., & Ferrara, A. 2018a, A&A, 619, 1
Padovani, M., Ivlev, A. V., Galli, D., & Caselli, P. 2018b, A&A, 614
Padovani, M., Ivlev, A. V., Galli, D., Offner, S. S., Indriolo, N., Rodgers-Lee, D., Marcowith, A., Girichidis, P., Bykov, A. M., & Diederik Kruijssen, J. M. 2020, Sp. Sci. Rev., 216, 29
Palla, F., Salpeter, E. E., & Stahler, S. W. 1983, ApJ, 271, 632
Parravano, A., Hollenbach, D. J., & McKee, C. F. 2003, ApJ, 584, 797
Peebles, P. J. E. & Dicke, R. H. 1968, ApJ, 154, 891
Prasad, S. S. & Huntress, W. T., J. 1980, ApJS, 43, 1
Ramaker, D. E. & Peek, J. M. 1976, Phys. Rev. A, 13, 58
Ranjan, A., Noterdaeme, P., Krogager, J.-K., Petitjean, P., Balashev, S. A., Bialy, S., Srianand, R., Gupta, N., Fynbo, J. P. U., Ledoux, C., & Laursen, P. 2018, A&A, 618, A184
Rémy-Ruyer, A., Madden, S. C., Galliano, F., Galametz, M., Takeuchi, T. T., Asano, R. S., Zhukovska, S., Lebouteiller, V., Cormier, D., Jones, A., Bocchio, M., Baes, M., Bendo, G. J., Boquien, M., Boselli, A., DeLooze, I., Doublier-Pritchard, V., Hughes, T., Karczewski, O. Ł., & Spinoglio, L. 2013, A&A, 563A, 31
Roberge, W. & Dalgarno, A. 1982, ApJ, 255, 489
Röllig, M., Ossenkopf, V., Jeyakumar, S., Stutzki, J., & Sternberg, A. 2006, A&A, 451, 917
Schneider, I. F., Dulieu, O., Giusti-Suzor, A., & Roueff, E. 1994, ApJ, 424, 983
Spitzer, L. & Tomasko, M. G. 1968, ApJ, 152, 971
Stancil, P. C. & Dalgarno, A. 1998, Faraday Discussions, 109, 61
Stancil, P. C., Lepp, S., & Dalgarno, A. 1998, ApJ, 509, 1
Sternberg, A. 1989, ApJ, 347, 863
Sternberg, A. & Dalgarno, A. 1995, ApJS, 99, 565
Sternberg, A., Petit, F. L., Roueff, E., & Bourlot, J. L. 2014, ApJS, 790, 10S
Tabone, B., Godard, B., des Forêts, G. P., Cabrit, S., & van Dishoeck, E. F. 2020, Molecule formation in dust-poor irradiated jets I. stationary disk winds
Tacconi, L. J., Genzel, R., & Sternberg, A. 2020, arXiv:2003.06245
Tegmark, M., Silk, J., Rees, M. J., Blanchard, A., Abel, T., & Palla, F. 1997, ApJ, 474, 1
Theard, L. P. & Huntress, W. T. 1974, J. Chem. Phys., 60, 2840
Tielens, A. G. G. M. 2013, Rev. Mod. Phys., 85, 1021
Tielens, A. G. G. M. & Hollenbach, D. 1985, ApJ, 291, 722
Turk, M. J., Oishi, J. S., Abel, T., & Bryan, G. L. 2012, ApJ, 745, 154
van Dishoeck, E. F. 2014, Faraday Discussions, 168, 9
Visbal, E., Haiman, Z., Terrazas, B., Bryan, G. L., & Barkana, R. 2014, MNRAS, 445, 107
Vranckx, S., Loreau, J., Desouter-Lecomte, M., & Vaeck, N. 2013, Journal of Physics B Atomic Molecular Physics, 46, 155201
Wakelam, V., Bron, E., Cazaux, S., Dulieu, F., Gry, C., Guillard, P., Habart, E., Hornekær, L., Morisset, S., Nyman, G., Pirronello, V., Price, S. D., Valdivia, V., Vidali, G., & Watanabe, N. 2017, Mol. Astrophys., 9, 1
Weingartner, J. C. & Draine, B. T. 2001, ApJS, 134, 263
Wolcott-Green, J., Haiman, Z., & Bryan, G. L. 2011, MNRAS, 418, 838
—. 2017, MNRAS, 469, 3329
Wolcott-Green, J., Haiman, Z., & Bryan, G. L. 2021, MNRAS, 500, 138
Wolfire, M. G., McKee, C. F., Hollenbach, D., & Tielens, A. G. G. M. 2003, ApJ, 587, 278

6. APPENDIX A: METALS, DUST, AND THE FRACTIONAL IONIZATION

In Equation (11) we are assuming that free electrons provided by the ionization of heavy elements are negligible, and that dust grains do not affect the hydrogen-helium chemistry and associated ionization fractions. In standard Galactic PDRs free electrons are produced by the photoionization of atomic carbon and other heavy elements with low ionization potentials. For example, in the outer CII zones, photoionization of atomic carbon provides an ionization floor of $x_{\rm e} \sim 2.6 \times 10^{-4}$ for solar metallicity (e.g., Sternberg & Dalgarno 1995). Eq. (11) is then valid for metallicities $Z' \lesssim 0.01(\zeta_{-16}/n_6)^{1/2}$. Photoionization of heavy elements in dust-free gas could enhance the gas-phase H_2 formation efficiency, but we do not consider such effects in this paper.

Charge transfer between dust grains and ions, or "dust-assisted recombination", may enhance the neutralization of gas phase ions, including H^+ and He^+ (Weingartner & Draine 2001). The presence of small dust particles (e.g. polycyclic aromatic hydrocarbons, PAHs) may further alter the gas phase ionization fractions via electron attachment and the formation of negatively charged dust particles (Lepp et al. 1988). For any ion, the dust-assisted recombination rate coefficient depends on the overall dust-to-gas ratio, and the grain charge. We recall that the dust-assisted recombination coefficient is a monotonically decreasing function of the grain charge parameter $\psi = I_{\rm LW}\sqrt{T}/n_e$, where n_e is the electron density. The grain-assisted recombination rate coefficient is maximal for small ψ. For Galactic dust abundances the maximal dust-assisted recombination rate for H^+ is $\alpha_g n$ where $\alpha_g \sim 10^{-13}$ cm^3 s^{-1} (Weingartner & Draine 2001). Dust recombination is therefore negligible for $Z'_d \lesssim x_{\rm e}\alpha_{\rm B}/\alpha_g \approx 1.9 \times 10^{-4}(\zeta_{-16}/n_6)^{1/2}$ at 100 K.

For the effects of small grains, we have verified by explicit computation for our model parameter space described in §4, that any PAHs are present mainly as neutral or negatively charged particles. We calculated the relative PAH^+/PAH/PAH^- abundances using the rate coefficients for recombination and attachment with electrons, and charge transfer reactions with H and H^+, as summarized in Wolfire et al. (2003) (see their Appendix C2), and the photoionization and photodetachment cross sections recommended by Lepp et al. (1988). For a characteristic PAH abundance $x_{\rm PAH,\odot} = 6 \times 10^{-7}$ for $Z'_d = 1$ (Lepp et al. 1988; Weingartner & Draine 2001) we find that the PAHs do not alter the hydrogen-helium chemistry and ionization structure for $Z'_d \lesssim 10^{-5}$. This can also be seen analytically. The dominant neutralization process is attachment ($\rm PAH + e \rightarrow PAH^- + \nu$), with a rate coefficient $\kappa_- = 1.34 \times 10^{-6}$ cm^3 s^{-1}. This reaction is negligible compared to radiative recombination with protons for $Z'_d \lesssim x_{\rm e}\alpha_{\rm B}/x_{\rm PAH,\odot}\kappa_- = 2.4 \times 10^{-5}(\zeta_{-16}/n_6)^{1/2}$. We conclude that for $\zeta_{-16} = n_6 = 1$ dust-grain neutralization and H_2 formation on dust surfaces (as discussed in §3.1) are, coincidentally, both negligible at dust-to-gas ratios $Z'_d \sim 10^{-5}$.

7. APPENDIX B: COMPARISON TO STERNBERG ET AL. 2014

As discussed in S14, in dusty *optically thick* PDRs the total HI column density maintained by photodissociation for beamed radiation is

$$N_{\rm HI,tot}^{\rm LW} = \frac{1}{\sigma_g}\ln[\frac{\alpha G}{2}+1] = \frac{1}{\sigma_g}\ln[\frac{1}{2}\frac{\sigma_g \bar{F}_{\nu,\rm LW} W_{g,\rm tot}}{R_{\rm dust} n}+1] \quad , \tag{41}$$

where the dimensionless parameters

$$\alpha \equiv \frac{D_0}{R_{\rm dust} n} \quad , \tag{42}$$

and

$$G \equiv \frac{\sigma_g}{\sigma_d} W_{g,\rm tot} \quad . \tag{43}$$

In these expressions, $\bar{F}_{\nu,\rm LW}$ is the mean LW band flux-density (photons cm^{-2} s^{-1} Hz^{-1}), σ_d is the total H_2 photodissociation cross section (cm^2 Hz), $D_0 = \sigma_d \bar{F}_{\nu,\rm LW}$ is the free-space photodissociation rate (s^{-1}), $W_{g,\rm tot}$ (Hz) is the total H_2-dust limited dissociation bandwidth (see S14), σ_g is the LW dust continuum absorption cross section (cm^2), $R_{\rm dust}$ is the dust-grain H_2 formation rate coefficient (cm^3 s^{-1}) and n is the gas density (cm^{-3}). The dimensionless parameter, α is the ratio of the free-space dissociation rate to the H_2 formation rate, and G (also dimensionless) is the dust-opacity averaged H_2 self-shielding factor (see Eq. 45 in S14).

In the strong field limit, $\alpha G \gtrsim 1$, and

$$N_{\rm HI,tot}^{\rm LW} \approx \frac{1}{\sigma_g}\ln[\frac{1}{2}\frac{\sigma_g \bar{F}_{\nu,\rm LW} W_{g,\rm tot}}{R_{\rm dust} n}] \quad . \tag{44}$$

In this limit, the HI-dust opacity $\sigma_g N_{\rm HI,tot}^{\rm LW}$ associated with the photodissociated HI column is large. The HI column is only logarithmically sensitive to αG because the HI column is self-limited by the HI-dust absorption that competes with H_2 photodissociations. The dominating HI-dust opacity leads to sharp HI-to-H_2 transitions due to the exponential dust reductions of the LW flux (see Fig. 7 in S14).

In the weak-field limit, $\alpha G \ll 1$, and

$$N_{\rm HI,tot}^{\rm LW} \approx \frac{1}{2}\frac{\bar{F}_{\nu,\rm LW} W_{g,\rm tot}}{R_{\rm dust} n} \quad . \tag{45}$$

In this limit HI-dust opacity is negligible, and the HI column is linear with αG, i.e. with the incident LW flux. The HI-to-H_2 transitions are controlled by H_2 self-shielding in non-overlapping absorption lines and the transitions are gradual (not sharp). In the weak-field limit a large fraction of the photodissociated HI column is built up past the transition points inside the molecular zones (see Fig. 7 in S14).

We now consider dust-free systems. For these, $\sigma_g \to 0$, and $W_{g,\rm tot} \to W_{d,\rm tot}$, where $W_{d,\rm tot}$ is the dust-free H_2 dissociation bandwidth. Thus, $G \to 0$. Furthermore, $R_{\rm dust}$ is replaced with a non-vansihing R_-. So for dust-free conditions αG is small by definition, and

$$N_{\rm HI,tot}^{\rm LW} \approx \frac{1}{2}\frac{\bar{F}_{\nu,\rm LW} W_{d,\rm tot}}{R_- n} \quad . \tag{46}$$

This is formally analogous to the weak-field limit (eq. [45]) for dusty clouds for which (a) HI dust opacity is negligible (b) the transitions are controlled by H_2 self-shielding, and (c) the HI is linearly proportional to the incident LW flux. However, for dust-free clouds a different distinction between weak and strong fields remains. For $N_{\rm HI,tot}^{\rm LW} \gtrsim 10^{22}$ cm^{-2}, which is the H_2 column density required for complete line-overlap, the HI-to-H_2 transitions are sharp due to the exponential cutoff of the dissociation rates. This is the strong-field limit for dust-free clouds. For $N_{\rm HI,tot}^{\rm LW} \lesssim 10^{22}$ cm^{-2}, the transitions occur before the absorption lines overlap. The conversions are then gradual with significant HI in the molecular zones up to the point where the lines finally do overlap and the LW band photons are fully absorbed. This is the weak-field limit for dust-free clouds. As discussed in §3.1 and Appendix A, for $\zeta_{-16}/n_6 \sim 1$ the dust-free limit is reached for dust-to-gas ratios $Z'_d \lesssim 10^{-5}$, and overall metallicities $Z' \lesssim 10^{-2}$, relative to characteristic Galactic values.